Channel Parameter Estimation in Mobile Radio Environments Using the SAGE Algorithm

Bernard H. Fleury, *Member, IEEE*, Martin Tschudin, *Student Member, IEEE*, Ralf Heddergott, *Student Member, IEEE*, Dirk Dahlhaus, *Member, IEEE*, and Klaus Ingeman Pedersen, *Student Member, IEEE*

***Abstract*— This study investigates the application potential of the SAGE (space-alternating generalized expectation-maximization) algorithm to jointly estimate the relative delay, incidence azimuth, Doppler frequency, and complex amplitude of impinging waves in mobile radio environments. The performance, i.e., high-resolution ability, accuracy, and convergence rate of the scheme, is assessed in synthetic and real macro- and pico-cellular channels. The results indicate that the scheme overcomes the resolution limitation inherent to classical techniques like the Fourier or beam-forming methods. In particular, it is shown that waves which exhibit an arbitrarily small difference in azimuth can be easily separated as long as their delays or Doppler frequencies differ by a fraction of the intrinsic resolution of the measurement equipment. Two waves are claimed to be separated when the mean-squared estimation errors (MSEE's) of the estimates of their parameters are close to the corresponding Cramér–Rao lower bounds (CRLB's) derived in a scenario where only a single wave is impinging. The adverb easily means that the MSEE's rapidly approach the CLRB's, i.e., within less than 20 iteration cycles. Convergence of the log-likelihood sequence is achieved after approximately ten iteration cycles when the scheme is applied in real channels. In this use, the estimated dominant waves can be related to a scatterer/reflector in the propagation environment.**

The investigations demonstrate that the SAGE algorithm is a powerful high-resolution tool that can be successfully applied for parameter extraction from extensive channel measurement data, especially for the purpose of channel modeling.

***Index Terms*—Antenna arrays, Cramér–Rao bound, direction of arrival, Doppler frequency, high-resolution array signal processing, maximum likelihood estimation, multipath channel, propagation delay, radio channel measurement and estimation, radio propagation.**

I. Introduction

FUTURE advanced mobile radio communication systems have to fulfill the increasing demand for transmission capacity. To meet this challenge, these systems may incorporate any form of diversity techniques. The optimization of the schemes implementing these techniques is only feasible provided that accurate channel models are made available to the system designers. Such models must reproduce in a realistic manner the entire dispersive behavior of the propagation channel, i.e., in delay, direction, Doppler, and polarization. Effective channel model elaboration relies on a realistic characterization of the probability distribution of the relevant channel parameters. This knowledge is gathered experimentally from comprehensive data collected during extensive measurement campaigns. Hence, sophisticated, accurate, and computationally efficient signal processing tools are required to extract the channel parameters of interest from the measurement data.

Recently, various high resolution methods have been proposed in mobile radio to estimate some of the parameters of impinging plane waves, i.e., their complex amplitude, relative delay, incidence azimuth, incidence elevation, and Doppler frequency. These methods can be grouped into three of the categories defined in [1]: spectral estimation, parametric subspace-based estimation (PSBE), and deterministic parametric estimation (DPE). Worth mentioning within the first category is the MUSIC (multiple signal classification) algorithm [2]. The ESPRIT (estimation of signal parameter via rotational invariance techniques) [3] and Unitary ESPRIT [4] methods belong to the PSBE techniques. All three mentioned methods were previously developed for azimuth estimation. The MUSIC algorithm was later applied to delay estimation [5]. The ESPRIT method has been recently adapted for joint delay and azimuth estimation [6], while the Unitary ESPRIT technique has been extended to perform joint azimuth and elevation estimation [7]. An application of the latter to process wide-band channel measurements is presented in [8]. Among the DPE methods, the expectation-maximization (EM) algorithm has been used for either delay or azimuth estimation [9]. The SAGE (space-alternating generalized EM) algorithm, which is an extension of the EM algorithm, has been applied for joint delay and azimuth estimation in time-invariant environments [10] as well as for joint delay, azimuth, and Doppler frequency estimation in time-variant environments [11]. A recent application of this scheme for the estimation of the delay, azimuth, and elevation is presented in [12].

In this paper, we present results of a detailed study of the performance of the SAGE algorithm described in [10] and [11]. The resolution ability, accuracy, and convergence rate of the scheme are assessed in both synthetic and real macro- and pico-cellular channels. Classical concepts from estimation theory like the root-mean-square estimation error (RMSEE) and the Cramér–Rao lower bound (CRLB) are

Manuscript received July 24, 1998; revised October 1, 1998 and November 10, 1998. This work was supported in part by Nokia Telecommunications and the European Union, ACTS program as part of the TSUNAMI II project, "Technology in Smart Antennas for Universal Advanced Mobile Infrastructure, Part Two." The work of B. Fleury was supported in part by CTE, ETHZ.

B. H. Fleury and K. I. Pedersen are with the Center for PersonKommunikation, Aalborg University, DK-9220 Aalborg, Denmark.

M. Tschudin, R. Heddergott, and D. Dahlhaus are with the Communication Technology Laboratory (CTL), ETHZ, CH-8092 Zurich, Switzerland.

Publisher Item Identifier S 0733-8716(99)02636-0.

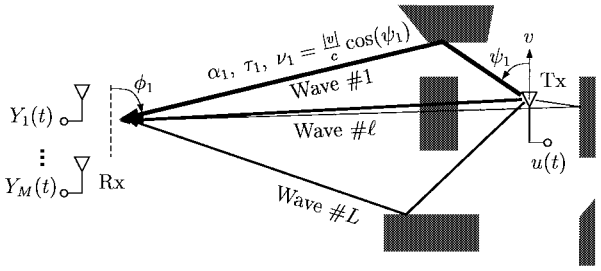

Fig. 1. Multipath propagation in mobile radio environments (v: speed of the mobile Tx, c: speed of light).

employed to describe the behavior of the SAGE algorithm in synthetic channels. When the SAGE algorithm is applied in real channels its performance assessment must rely on other criteria such as convergence of the log-likelihood sequence, goodness-of-fit between the power profiles calculated from the measurement data and those reconstructed based on the channel estimates, and the correspondence between the estimated waves and the propagation environment.

The paper is organized as follows. The underlying signal model is outlined in Section II. The description of the SAGE algorithm is sketched in Section III. Section IV is devoted to some relevant issues related to the implementation of the SAGE algorithm. The results concerning the performance of the scheme are presented in Sections V and VI.

II. Signal Model

The transmitted signal $u(t)$ consists of a periodically repeated burst signal $a(t)$: $u(t) = \sum_{i=-\infty}^{\infty} a(t - iT_a)$. The burst signal is of the form $a(t) = \sum_{k=0}^{K-1} a_k\, p(t - kT_p)$, where $[a_0, \ldots, a_{K-1}]$ and $p(t)$ denote, respectively, the (possibly complex) sounding sequence of length K and the shaping pulse whose duration T_p is related to T_a according to $T_a = KT_p$. The sounding signal $u(t)$ has power P_u.

The receiver (Rx) is equipped with an antenna array consisting of M sensors located at $r_1, \ldots, r_M \in \mathbb{R}^2$ with respect to an arbitrary reference point. As illustrated in Fig. 1, it is assumed in the underlying channel model that a finite number L of specular plane waves are impinging at the Rx location. The contribution of the ℓth wave to the M baseband signals at the output of the array can be expressed in vector notation as

$$\begin{aligned} s(t;\theta_\ell) &\triangleq [s_1(t;\theta_\ell), \ldots, s_M(t;\theta_\ell)]^{\mathrm{T}} \\ &= c(\phi_\ell)\alpha_\ell \exp\{\jmath 2\pi\nu_\ell t\} u(t - \tau_\ell) \end{aligned} \tag{1}$$

where $\theta_\ell \triangleq [\tau_\ell, \phi_\ell, \nu_\ell, \alpha_\ell]$ is the vector containing the parameters of the ℓth wave. The wave is characterized by its relative delay τ_ℓ, incidence azimuth ϕ_ℓ, Doppler frequency ν_ℓ, and complex amplitude α_ℓ. The M-dimensional (M-D) vector-valued function $c(\phi) \triangleq [c_1(\phi), \ldots, c_M(\phi)]^{\mathrm{T}}$ is the steering vector of the array. Its components are given by $c_m(\phi) \triangleq f_m(\phi)\exp\{\jmath 2\pi\lambda^{-1}\langle e(\phi), r_m\rangle\}$ with λ, $e(\phi)$, $f_m(\phi)$ denoting the wavelength, the unit vector in $\mathbb{R}^2$ pointing toward the direction determined by ϕ, and the complex electric field pattern of the mth sensor, respectively. The meaning of the vector operators arising in the above mathematical expressions is as follows: $[\cdot]^{\mathrm{T}}$ denotes transposition and $\langle \cdot, \cdot \rangle$ is the scalar product in $\mathbb{R}^2$. In the sequel we shall also make use of the notation $[\cdot]^*$ and $[\cdot]^{\mathrm{H}} \triangleq [[\cdot]^*]^{\mathrm{T}}$ for the complex conjugation and Hermitian operators.

We implicitly make the following simplifications when we write (1): First, the ratio of the array dimension to the velocity of light is much smaller than the inverse of the bandwidth of $u(t)$ so that the propagation duration of the waves within the array can be neglected. Second, for the sake of simplifying the presentation, the waves are assumed to propagate horizontally. This assumption proves to be realistic in macro-cells where the distance between the transmitter (Tx) and the Rx is usually large compared to the height difference between their antennas. In micro- and pico-cells the incidence elevation becomes significant and introduces an error in the azimuth estimation if it is discarded [8]. This effect is especially pronounced when linear antenna arrays are used. For this reason a circular array has instead been employed in the investigated pico-cellular environment. For such arrays the error in the azimuth estimation which results from discarding the elevation can be shown to be negligible small as long as the elevation is confined within $\pm 40^\circ$. Since the Rx and Tx are in line of sight and their antennas are at about the same height in the investigated environment the relevant impinging waves at the Rx are very likely to exhibit an incidence elevation within this range. Thus, discarding the elevation has no noticeable impact on the azimuth estimates. An extension of the model to include the elevation as well is presented in [12].

The received signal vector $Y(t) \triangleq [Y_1(t), \ldots, Y_M(t)]^{\mathrm{T}}$ at the output of the antenna array reads

$$Y(t) = \sum_{\ell=1}^{L} s(t;\theta_\ell) + \sqrt{\frac{N_0}{2}} N(t). \tag{2}$$

In this expression $N(t) \triangleq [N_1(t), \ldots, N_M(t)]^{\mathrm{T}}$ denotes a standard M-D vector-valued complex white Gaussian noise, i.e., $N_m(t) = N_{m\Re}(t) + \jmath N_{m\Im}(t)$, $m = 1, \ldots, M$, where $N_{1\Re}(t), N_{1\Im}(t), \ldots, N_{M\Re}(t), N_{M\Im}(t)$ are independent real zero-mean white Gaussian noise processes with unit spectral height. Moreover, N_0 is a positive constant. According to the above definition the noise is spatially independent. To keep a compact notation we also define

$$s(t;\theta) \triangleq \sum_{\ell=1}^{L} s(t;\theta_\ell) \tag{3}$$

where $\theta \triangleq [\theta_1, \ldots, \theta_L]$.

III. EM-Based Estimation of Superimposed Signals

A. Maximum Likelihood Estimation

The problem at hand is the estimation of the number L of waves as well as their parameter vectors $\theta_\ell = [\tau_\ell, \phi_\ell, \nu_\ell, \alpha_\ell]$, $\ell = 1, \ldots, L$. The estimation of L is not addressed in the paper. This parameter is fixed to a value large enough to capture all the dominant impinging waves. Classical information theoretic methods for model selection like Akaike's and Rissanen's criteria [13] can be used to estimate L.

The received signal $Y(t)$ is observed over a window consisting of I regularly spaced time intervals of duration T_a each. The spacing between the centers of two consecutive observation intervals is denoted by T_f, where $T_f \geq T_a$. The observation duration and the observation span are IT_a and $(I-1)T_f + T_a$, respectively. The reason why the received signal is not continuously observed, i.e., $T_f = T_a$, is that the absolute Doppler frequency of the impinging waves is considerably smaller than the inverse of the burst duration T_a. Hence, selecting $T_f > T_a$ makes it possible to increase the observation span, which leads to an enhancement of the Doppler resolution, while limiting the growth of the observation duration and therefore of the amount of measured data to be stored. By the Sampling Theorem $1/T_f$ must be larger than twice the maximum occurring Doppler frequency, while I must be confined in such a way that the observation span is smaller than the time interval during which the parameters of the waves remain approximately constant. The observation window is expressed with respect to its center of gravity as $D_o = \bigcup_{i=1}^{I}[(i-((I+1)/2))T_f - (T_a/2), (i-((I+1)/2))T_f + (T_a/2))$.

The log-likelihood function of $\theta = [\theta_1, \ldots, \theta_L]$ given an observation $Y(t) = y(t)$ over D_o is [14]

$$\Lambda(\theta; y) \triangleq \frac{1}{N_0}\left[2\int_{D_o} \Re\{s^{\mathrm{H}}(t';\theta)y(t')\}\,dt' - \int_{D_o} \|s(t';\theta)\|^2\,dt'\right]. \tag{4}$$

Here $\Re\{\cdot\}, \Im\{\cdot\}$, and $\|\cdot\|$ denote, respectively, the real part, the imaginary part, and the norm of the argument. Notice that given θ the only random element in (2) is the white noise $N(t)$. The maximum likelihood estimate (MLE) of θ is a value of this vector for which the function $\theta \mapsto \Lambda(\theta; y)$ is maximum

$$\hat{\theta}_{\mathrm{ML}}(y) \in \arg\max_{\theta}\{\Lambda(\theta; y)\}. \tag{5}$$

The calculation of $\hat{\theta}_{\mathrm{ML}}(y)$ is computationally prohibitive due to the high dimension of θ for large L and because no closed formula exists which expresses the global maxima of the nonlinear function $\theta \mapsto \Lambda(\theta; y)$. Since the values of the complex amplitudes maximizing $\Lambda(\theta; y)$ can be expressed in closed form as a function of the other parameters, the computation of the MLE of θ is a $3L$-D nonlinear optimization procedure.

B. The EM-Algorithm

The EM algorithm [15], [16], has been formulated by Dempster *et al.* [17] as a unifying iterative method for solving the ML estimation problem in situations where a part of the observations are missing or censored. In [9] the EM algorithm has been applied to the problem of estimating superimposed signals in white Gaussian noise. In this subsection we shall sketch the rationales, notions, and main properties of the EM algorithm that are needed for the presentation of the SAGE algorithm in Section III-C.

The derivation of the EM algorithm relies on the two key notions of the complete (unobservable) and incomplete (observable) data. In the problem of estimating superimposed signals (2), the individual signals $s(t;\theta_\ell)$ corrupted by a part of the additive noise, i.e.,

$$X_\ell(t) \triangleq s(t;\theta_\ell) + \sqrt{\frac{\beta_\ell N_0}{2}}\,N_\ell(t), \qquad \ell = 1, \ldots, L \tag{6}$$

constitute a natural set of complete data [9] (see Fig. 2). Here, $N_1(t), \ldots, N_L(t)$ are independent standard M-D complex white Gaussian noises. The nonnegative parameters $\beta_1, \ldots, \beta_L$ satisfy $\Sigma_{\ell=1}^{L}\beta_\ell = 1$ so that the set $\{\sqrt{\beta_1}N_1(t), \ldots, \sqrt{\beta_L}N_L(t)\}$ forms a decomposition of $N(t)$. The received signal $Y(t)$ is identified with the incomplete data. It is related to the complete data according to $Y(t) = \Sigma_{\ell=1}^{L}X_\ell(t)$.

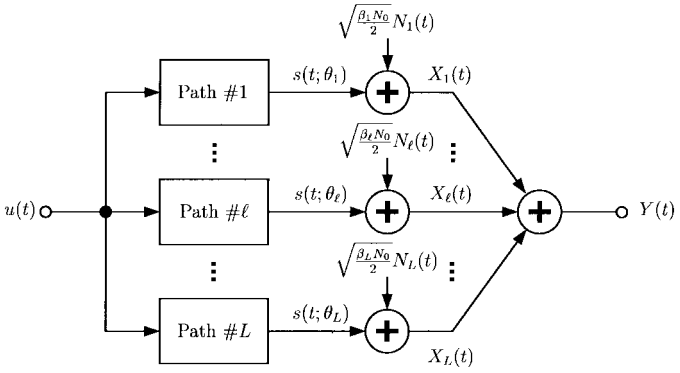

Fig. 2. Relation between the complete and incomplete data.

To figure out the rationale leading to the EM algorithm, let us assume for the moment that the complete data can be observed. Since $X_1(t), \ldots, X_L(t)$ are independent, the components $X_{\ell'}, \ell' \neq \ell$ are irrelevant [18] for the estimation of θ_ℓ. The log-likelihood function of θ_ℓ for the observation $X_\ell(t) = x_\ell(t)$ over D_o has a form similar to that in (4)

$$\Lambda(\theta_\ell; x_\ell) \triangleq \frac{1}{\beta_\ell N_0}\left[2\int_{D_o} \Re\{s^{\mathrm{H}}(t';\theta_\ell)x_\ell(t')\}\,dt' - \int_{D_o} \|s(t';\theta_\ell)\|^2\,dt'\right]. \tag{7}$$

The MLE of θ_ℓ for the observation $X_\ell(t) = x_\ell(t)$ is given as $(\hat{\theta}_\ell)_{\mathrm{ML}}(x_\ell) \in \arg\max_{\theta_\ell}\{\Lambda(\theta_\ell; x_\ell)\}$. Since $X_\ell(t)$ is not observable one can try to estimate it based on the observation $Y(t) = y(t)$ of the incomplete data and a previous estimate $\hat{\theta}'$ of θ. A natural estimate of $X_\ell(t)$ is its conditional expectation given $Y(t) = y(t)$ and assuming $\theta = \hat{\theta}'$

$$\hat{x}_\ell\left(t;\hat{\theta}'\right) \triangleq \boldsymbol{E}_{\hat{\theta}'}[X_\ell(t)|y] \qquad (\ell = 1, \ldots, L) \tag{8}$$

where $\boldsymbol{E}_\theta[\cdot]$ denotes expectation assuming the parameter value θ. The wave parameter vector θ_ℓ can then be re-estimated by computing its MLE based on the observation $X_\ell(t) = \hat{x}_\ell(t;\hat{\theta}')$

$$\hat{\theta}''_\ell = \left(\hat{\theta}_\ell\right)_{\mathrm{ML}}\left(\hat{x}_\ell\left(t;\hat{\theta}'\right)\right) \qquad (\ell = 1, \ldots, L). \tag{9}$$

The computations of (8) and (9) are referred to as the Expectation (E) step and the Maximization (M) step, respectively, of the EM algorithm. For any initial value $\hat{\theta}(0)$, a sequence of estimates $\{\hat{\theta}(\mu)\} \triangleq \{\hat{\theta}(\mu)\colon \mu = 0, 1, \ldots\}$ is generated by iteratively carrying out these two steps, where at each iteration

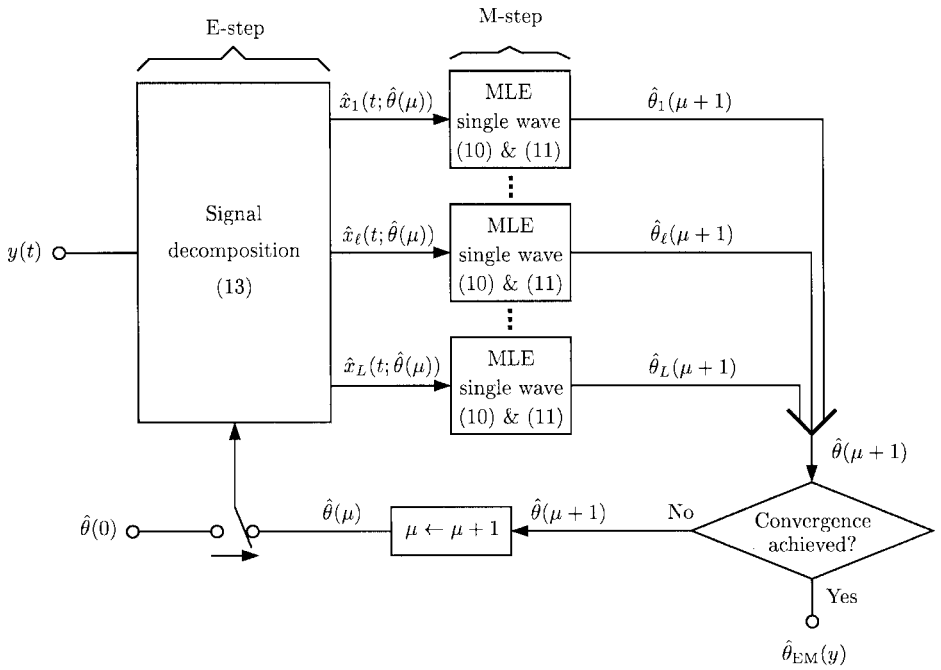

Fig. 3. Signal flow graph of the EM algorithm.

μ the identifications $\hat{\theta}' = \hat{\theta}(\mu)$ and $\theta'_\ell = \theta_\ell(\mu+1)$, $\ell = 1,\ldots,L$, are made. The signal flow graph (SFG) of the EM algorithm is depicted in Fig. 3. Inspection of this figure shows that the EM algorithm allows the splitting of the optimization problem required to jointly estimate L superimposed waves into L separate optimization problems for estimating a single impinging wave.

The EM algorithm has the remarkable property that for any generated sequence $\{\hat{\theta}(\mu)\}$, the sequence of log-likelihood values $\{\Lambda(\hat{\theta}(\mu);y)\}$ cannot decrease (monotonicity property) [17]. Moreover the sequence converges to a stationary point provided the iteration function $(\theta_\ell,\hat{\theta}') \mapsto \Lambda(\theta_\ell;\hat{x}_\ell(t;\hat{\theta}'))$ which is needed to compute (9) satisfies some weak regularity conditions [15]. In practice, the iteration process is stopped as soon as the distance between the parameter estimates returned by the EM algorithm at two consecutive iteration steps is below a predefined threshold or when the sequence $\{\Lambda(\hat{\theta}(\mu);y)\}$ has stabilized.

1) ML Estimation of a Single Impinging Wave: We now derive the MLE $(\hat{\theta}_\ell)_{\mathrm{ML}}(x_\ell)$. Upon insertion of (3) and (1) in (7) it can be shown that the value of α_ℓ that maximizes $\Lambda(\theta_\ell;x_\ell)$ can be derived in a closed form as a function of $[\tau_\ell,\phi_\ell,\nu_\ell]$ [11]. Substitution of this value for α_ℓ in $\Lambda(\theta_\ell;x_\ell)$ yields the following procedure for the computation of $(\hat{\theta}_\ell)_{\mathrm{ML}}(x_\ell)$.

MLE's of the parameters of a single impinging wave:

$$\left(\tau_\ell,\widehat{\phi_\ell},\nu_\ell\right)_{\mathrm{ML}}(x_\ell) = \arg\max_{[\tau,\phi,\nu]}\{|z(\tau,\phi,\nu;x_\ell)|\} \tag{10}$$

$$(\hat{\alpha}_\ell)_{\mathrm{ML}}(x_\ell) = \frac{1}{I||c((\hat{\phi}_\ell)_{\mathrm{ML}}(x_\ell))||^2 T_a P_u} \cdot z\left(\left(\tau_\ell,\widehat{\phi_\ell},\nu_\ell\right)_{\mathrm{ML}}(x_\ell);x_\ell\right) \tag{11}$$

where

$$\begin{aligned} z(\tau,\phi,\nu;x_\ell) &\triangleq \int_{D_o} u^*(t'-\tau)\exp\{-\jmath 2\pi\nu t'\} \\ &\quad \cdot c^{\mathrm{H}}(\phi)x_\ell(t')\,dt' \\ &= \sum_{i=1}^{I}\int_{D_i} u^*(t'-\tau)\exp\{-\jmath 2\pi\nu t'\} \\ &\quad \cdot c^{\mathrm{H}}(\phi)x_\ell(t')\,dt'. \end{aligned} \tag{12}$$

Notice that $||c(\phi)||^2 = \Sigma_{m=1}^{M}\ |f_m(\phi)|^2$. A possible SFG for computing the function $z(\tau,\phi,\nu;x_\ell)$ is given in Fig. 4. According to (10) and (11) the MLE's of the parameters of the ℓth wave are obtained by simultaneously varying τ, ϕ, and ν within their respective range until the magnitude of the signal at the output of the SFG is maximum. The resulting triple then equals $(\tau_\ell,\widehat{\phi_\ell},\nu_\ell)_{\mathrm{ML}}(x_\ell)$, while $(\hat{\alpha}_\ell)_{\mathrm{ML}}(x_\ell)$ is the output signal normalized by a system-dependent factor.

2) Estimation of the Complete Data: The estimate $\hat{x}_\ell(t;\hat{\theta}')$ of the complete data $X_\ell(t)$ in (8) is expressed as [9]

$$\hat{x}_\ell\left(t;\hat{\theta}'\right) = s\left(t;\hat{\theta}'_\ell\right) + \beta_\ell\left[y(t) - \sum_{\ell'=1}^{L} s(t;\hat{\theta}'_{\ell'})\right]. \tag{13}$$

The first term is the contribution of the ℓth impinging wave assuming $\theta_\ell = \hat{\theta}'_\ell$. The expression within the brackets is an estimate of the noise $\sqrt{\frac{N_0}{2}}N(t)$ based on the hypothesis that $\theta = \hat{\theta}'$. Since the calculation of the right-hand terms in (11) and (13) is simple, the complexity of the EM algorithm is L times the complexity of the three-dimensional (3-D) optimization procedure (10). Apart from the constraint $\Sigma_{\ell=1}^{L}\beta_\ell = 1$, the nonnegative coefficients β_ℓ are free parameters that should be selected to maximize the convergence rate of the EM

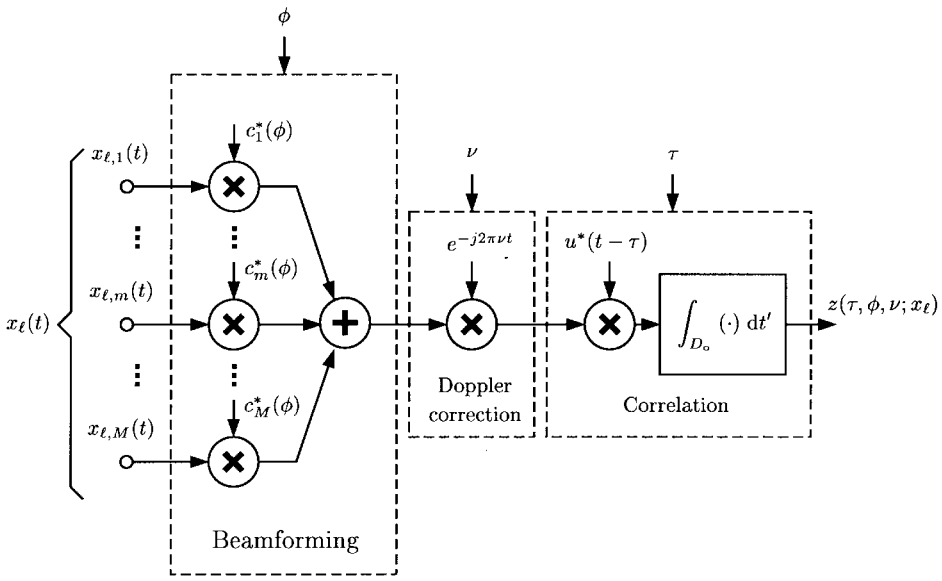

Fig. 4. A possible implementation of $z(\tau,\phi,\nu;x_\ell)$ in (12).

algorithm and to possibly avoid convergence to an unwanted stationary point [9].

C. The SAGE Algorithm

The SAGE algorithm [19] is a twofold extension of the EM algorithm. First, each iteration of the SAGE algorithm is an EM iteration to re-estimate not necessarily all but only a subset of the components of θ while keeping the estimates of the other components fixed. Admissible hidden data are associated which each of these parameter subsets. Data are admissible for a given subset if they are complete for this subset under the hypothesis that the components of θ belonging to the complement of this subset are known. Second, the notion of complete data is generalized in the sense that the mapping from the complete data space to the incomplete data space may be random rather than deterministic as originally considered in [17]. The selection of admissible data guarantees that the SAGE algorithm retains the monotonicity property of the EM algorithm [19]. The SAGE algorithm is actually a grouped coordinate ascent method. Faster convergence for a correspondingly lower complexity is the advantage of the SAGE algorithm compared to the EM algorithm [19].

The details concerning the application of the SAGE algorithm to the resolution of electromagnetic waves can be found in [10] and [11]. To avoid the introduction of additional symbolic notations we shall in this section sometimes identify the vectors θ_ℓ and θ with the set of their components. In the problem of estimating superimposed signals, natural parameter subsets comprise all the parameters of the individual signals, i.e., are $\theta_1,\ldots,\theta_L$. In fact this selection is well suited as $X_\ell(t)$ in (6) is admissible for θ_ℓ. Moreover, it can be seen that $\beta_\ell = 1$ maximizes the conditional Fisher information of $X_\ell(t)$ given $Y(t) = y(t)$. Maximizing this matrix proves to maximize the asymptotic convergence rate of the EM algorithm [17]. Moreover, empirical evidence shows that this choice also leads to a fast convergence of the algorithm already in the early iteration steps [19]. The SFG of the resulting SAGE algorithm is given in Fig. 5. The M-step is still the ML procedure for a single wave, which is applied to the estimate of $X_\ell(t)$ given in (13) with $\beta_\ell = 1$. Notice that at the μth iteration step the parameters of the wave $\ell = \mu \bmod(L)+1$ are re-estimated. We define an iteration cycle of the SAGE algorithm as L consecutive iteration steps for updating the parameter estimates of all waves once. The computational complexity of one iteration step of the EM algorithm is identical to that of one iteration cycle of the SAGE algorithm.

To further reduce the complexity of the SAGE algorithm described above we aim at replacing the 3-D optimization procedure (10) to compute the MLE of the parameters of one single wave by three separate one-dimensional (1-D) procedures, where each parameter is estimated individually. This can also be formulated within the SAGE framework by further splitting each subset θ_ℓ, $\ell = 1\ldots L$, into the three subsets $\{\tau_\ell,\alpha_\ell\}$, $\{\phi_\ell,\alpha_\ell\}$, and $\{\nu_\ell,\alpha_\ell\}$. The random process (6) is still admissible for each of these subsets, and the conditional Fisher information is still maximized with $\beta_\ell = 1$. Concatenation of the three SAGE iterations for re-estimating the pairs in the three subsets above yields the following updating procedure.

Coordinate-wise updating procedure of the parameter estimates of one wave:

$$\begin{aligned}
\hat\tau_\ell'' &= \arg\max_\tau \left\{\left|z\left(\tau,\hat\phi_\ell',\hat\nu_\ell';\hat x_\ell\left(t;\hat\theta'\right)\right)\right|\right\}\\
\hat\phi_\ell'' &= \arg\max_\phi \left\{\left|z\left(\hat\tau_\ell'',\phi,\hat\nu_\ell';\hat x_\ell\left(t;\hat\theta'\right)\right)\right|\right\}\\
\hat\nu_\ell'' &= \arg\max_\nu \left\{\left|z\left(\hat\tau_\ell'',\hat\phi_\ell'',\nu;\hat x_\ell\left(t;\hat\theta'\right)\right)\right|\right\}\\
\hat\alpha_\ell'' &= \frac{1}{I\|c(\hat\phi_\ell'')\|^2 T_a P_u} z\left(\hat\tau_\ell'',\hat\phi_\ell'',\hat\nu_\ell'';\hat x_\ell\left(t;\hat\theta'\right)\right). \qquad (14)
\end{aligned}$$

This updating procedure can be performed by applying the SFG in Fig. 4 to the signal $\hat x_\ell(t;\hat\theta')$. The updated estimates $\hat\tau_\ell''$, $\hat\phi_\ell''$, and $\hat\nu_\ell''$ are obtained by successively varying τ, ϕ, and ν until the magnitude of the signal at the output of the SFG

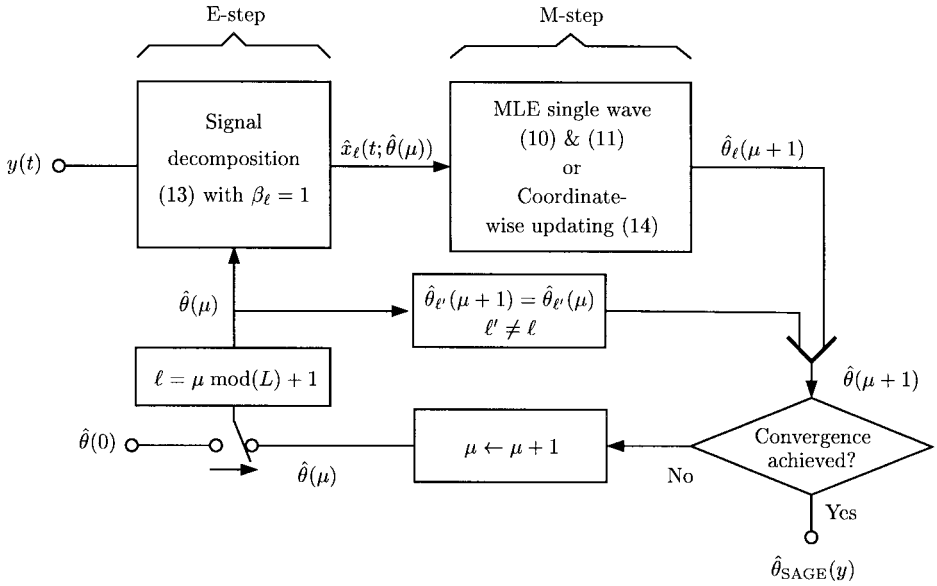

Fig. 5. Signal flow graph of the SAGE algorithm.

is maximum. The updated amplitude estimate $\hat{\alpha}''_\ell$ is then the output signal normalized by the system-dependent factor.

The SFG of the SAGE algorithm which results from the above particular choice of parameter subsets and their admissible data is also that depicted in Fig. 5 with the M-step given by (14). Obviously, this algorithm reduces to a coordinate ascent method in this case.

IV. Implementation Issues

A. Simplification for Low Doppler Frequencies

In the mobile environment the magnitude of the Doppler frequency of the impinging waves is much smaller than $1/T_a$. Thus, the phase term $2\pi\nu_\ell t$ in (1) can be approximated by a constant term according to $2\pi\nu_\ell t \approx 2\pi(i-((I+1)/2))\nu_\ell T_f$ over each observation interval $D_i \triangleq [(i-((I+1)/2))T_f - (T_a/2), (i-((I+1)/2))T_f + (T_a/2))$, $i = 1,\ldots,I$, of D_o. Inserting the right-hand term above in (1) yields the following approximation for $s(t;\theta_\ell)$ over D_i

$$s(t;\theta_\ell) \approx c(\phi_\ell)\alpha_\ell \exp\left\{\jmath 2\pi\left(i-\frac{I+1}{2}\right)\nu_\ell T_f\right\} u(t-\tau_\ell), \quad t \in D_i. \tag{15}$$

B. Initialization of the SAGE Algorithm

Two methods are proposed to initialize the SAGE algorithm. The first one can be included in SFG the SAGE algorithm as follows: One "initialization" cycle with the iteration step μ ranging in $\{-(L-1),\ldots,0\}$ is performed starting with the pre-initial setting $\hat{\theta}(-L) = [0,\ldots,0]$. Since no *a priori* knowledge about the phase of the complex amplitudes is available noncoherent estimation of the delays and azimuths is performed. To this aim, the first two maximization procedures in (14) are replaced by

$$\hat{\tau}''_\ell = \arg\max_\tau \left\{\sum_{m=1}^{M}\sum_{i=1}^{I}\left|\int_{D_i} u^*(t'-\tau)\hat{x}_{\ell,m}(t';\hat{\theta}')\,dt'\right|^2\right\} \tag{16}$$

$$\hat{\phi}''_\ell = \arg\max_\phi \left\{\sum_{i=1}^{I}\left|\int_{D_i} u^*(t'-\hat{\tau}''_\ell)c^{\mathrm{H}}(\phi)\hat{x}_\ell(t;\hat{\theta}')\,dt'\right|^2\right\} \tag{17}$$

during the initialization cycle. At step $\mu \in \{-(L-1),\ldots,0\}$, the parameter estimates of wave $\ell = L+\mu$ are initialized and $\hat{\theta}(\mu-1) = [\hat{\theta}_1 - (L-1),\ldots,\hat{\theta}_{\ell-1}(\ell-L-i),0,\ldots,0]$. Inserting $\hat{\theta}(\mu-1)$ in (13) yields the estimate $\hat{x}_\ell(t;\hat{\theta}(\mu-1)) = y(t) - \Sigma_{\ell'=1}^{\ell-1}\, s(t;\hat{\theta}_{\ell'}(\ell'-L))$ of the hidden data $X_\ell(t)$ that is used in the modified M-step to calculate $\hat{\theta}_\ell(\mu)$. Thus, signal estimates of the waves whose parameter estimates have already been initialized are subtracted from the observed signal $y(t)$. Such a technique is commonly referred to as successive interference cancellation.

In the second method all initial estimates of the delays are first computed by using the MUSIC algorithm proposed in [5]. An initialization cycle of the SAGE algorithm is then carried out to compute the initial estimate of the remaining wave parameters. During this initialization cycle the updating procedure (14) is modified as follows: The first maximization procedure is discarded while the second one is replaced by (17) $\hat{x}_\ell(t;\hat{\theta}')$. Hence, being replaced by $y(t)$, no cancellation is carried out in this case.

V. Performance in Synthetic Channels

A. Cramér–Rao Lower Bound for the Estimation of L Waves

For the subsequent investigation it is worth considering the real $5L$-D vector

$$\Omega \triangleq [\Re\{\alpha_1\},\ldots,\Re\{\alpha_L\},\Im\{\alpha_1\},\ldots,\Im\{\alpha_L\}, \tau_1,\ldots,\tau_L,\phi_1,\ldots,\phi_L,\nu_1,\ldots,\nu_L] \tag{18}$$

instead of θ. The information inequality for the covariance matrix of any unbiased estimate $\hat{\Omega}$ reads [20]

$$\boldsymbol{E}_{\Omega}\left[\left(\hat{\Omega}-\Omega\right)^{\mathrm{T}}\left(\hat{\Omega}-\Omega\right)\right] \geq F^{-1}(\Omega) \tag{19}$$

where the $5L\times 5L$ positive definite real matrix $F(\Omega)$ is the so-called Fisher information matrix (FIM) of Ω. If $\hat{\Omega}_k$ is unbiased its mean-square estimation error (MSEE) is lower-bounded as

$$\begin{aligned}\mathrm{MSEE}(\hat{\Omega}_k) &\triangleq \boldsymbol{E}_{\Omega}\left[(\hat{\Omega}_k-\Omega_k)^2\right] \\ &\geq \left[F^{-1}(\Omega)\right]_{kk} \triangleq \mathrm{CRLB}(\Omega_k).\end{aligned} \tag{20}$$

The diagonal element $[F^{-1}(\Omega)]_{kk}$ of $F^{-1}(\Omega)$ is referred to as the CRLB of $\hat{\Omega}_k$. In addition, we define the root MSEE (RMSEE) of $\hat{\Omega}_k$ as $\mathrm{RMSEE}(\hat{\Omega}_k) \triangleq \sqrt{\mathrm{MSEE}(\hat{\Omega}_k)}$. When the estimator is biased, its MSEE is bounded from below according to [21]

$$\begin{aligned}\boldsymbol{E}_{\Omega}\left[(\hat{\Omega}_k-\Omega_k)^2\right] \geq [b(\Omega)]_k^2 + \big[(I+\nabla_{\Omega} b(\Omega)) \\ \cdot F^{-1}(\Omega)\,(I+\nabla_{\Omega} b(\Omega))^T\big]_{kk}\end{aligned} \tag{21}$$

where $b(\Omega) \triangleq \boldsymbol{E}_{\Omega}[\hat{\Omega}]-\Omega$ denotes the bias of $\hat{\Omega}$ and $\nabla_{\Omega} b(\Omega)$ is the gradient of $b(\Omega)$. The sign of this gradient and the magnitude of the bias itself determine whether the bound (21) is larger or smaller than that in (20). Since $b(\Omega)$ is not known explicitly, (21) cannot be computed. However we shall regard the CRLB of an arbitrary estimate (20) as a benchmark to which its MSEE is compared.

We now derive $\mathrm{CRLB}(\Omega_k)$ in (20). It is shown in Appendix A that the elements of $F(\Omega)$ can be expressed as

$$F_{kk'}(\Omega) = \frac{2}{N_0}\,\Re\left\{\int_{D_o} \frac{\partial}{\partial\Omega_k} s^{\mathrm{H}}(t';\Omega)\,\frac{\partial}{\partial\Omega_{k'}} s(t';\Omega)\,dt'\right\}. \tag{22}$$

The following partition of the FIM in $L\times L$ submatrices will be useful for the subsequent treatment

$$F(\Omega) = \begin{bmatrix} F_{\Re\Re}(\Omega) & F_{\Re\Im}(\Omega) & F_{\Re\tau}(\Omega) & F_{\Re\phi}(\Omega) & F_{\Re\nu}(\Omega) \\ F_{\Re\Im}^{\mathrm{T}}(\Omega) & F_{\Im\Im}(\Omega) & F_{\Im\tau}(\Omega) & F_{\Im\phi}(\Omega) & F_{\Im\nu}(\Omega) \\ F_{\Re\tau}^{\mathrm{T}}(\Omega) & F_{\Im\tau}^{\mathrm{T}}(\Omega) & F_{\tau\tau}(\Omega) & F_{\tau\phi}(\Omega) & F_{\tau\nu}(\Omega) \\ F_{\Re\phi}^{\mathrm{T}}(\Omega) & F_{\Im\phi}^{\mathrm{T}}(\Omega) & F_{\tau\phi}^{\mathrm{T}}(\Omega) & F_{\phi\phi}(\Omega) & F_{\phi\nu}(\Omega) \\ F_{\Re\nu}^{\mathrm{T}}(\Omega) & F_{\Im\nu}^{\mathrm{T}}(\Omega) & F_{\tau\nu}^{\mathrm{T}}(\Omega) & F_{\phi\nu}^{\mathrm{T}}(\Omega) & F_{\nu\nu}(\Omega) \end{bmatrix}. \tag{23}$$

By analogy with $c(\phi)$ we define $d(\nu) \triangleq [d_1(\nu),\ldots,d_I(\nu)]^{\mathrm{T}}$ where $d_i(\nu) \triangleq \exp\{j2\pi(i-(I+1/2))\nu T_f\}$ [cf. (15)]. Moreover

$$\begin{aligned}\rho(\tau) &\triangleq \frac{1}{T_a P_u}\int_0^{T_a} u^*(t'-\tau)a(t')\,dt' \\ \zeta(\phi,\tilde{\phi}) &\triangleq \frac{1}{M}c^{\mathrm{H}}(\phi)c(\tilde{\phi}) \\ \eta(\nu,\tilde{\nu}) &\triangleq \frac{1}{I}d^{\mathrm{H}}(\nu)d(\tilde{\nu})\end{aligned} \tag{24}$$

are the delay, azimuth, and Doppler frequency correlation function of the measurement equipment, respectively. Note that $\rho(\tau) \leq 1$, $|\zeta(\phi,\tilde{\phi})| \leq (1/M)\|c(\phi)\|\,\|c(\tilde{\phi})\|$, and $|\eta(\nu,\tilde{\nu})| \leq 1$ with equality if $\tau=0$, $\phi=\tilde{\phi}$, and $\nu=\tilde{\nu}$, respectively. Furthermore, $\rho(\tau)$ is the periodic autocorrelation function of $a(t)$. To avoid aliasing, all signals are bandlimited to $1/2T_s$ prior to sampling at the rate $1/T_s = N_s/T_p$, where N_s denotes the number of samples per pulse duration. It is shown in Appendix B that we can rewrite (22) according to

$$\begin{aligned}F_{kk'}(\Omega) = 2\gamma\Re\Big\{\frac{\partial}{\partial\Omega_k}\,\frac{\partial}{\partial\Omega_{k'}}\alpha_{\ell}^*\alpha_{\ell'}\rho(\tau_{\ell}-\tau_{\ell'}) \\ \cdot\ \zeta(\phi_{\ell},\phi_{\ell'})\eta(\nu_{\ell},\nu_{\ell'})\Big\}\end{aligned} \tag{25}$$

with $\gamma \triangleq (MIT_aP_u/N_0)$. The indexes ℓ and ℓ' are obtained from k and k' according to $\ell = (k-1) \bmod(L)+1$ and $\ell' = (k'-1) \bmod(L)+1$, respectively.

The subsequent investigations focus on uniform linear arrays with $\lambda/2$ spaced omnidirectional sensors, i.e., $f_m(\phi)=1$, $m=1,\ldots,M$. The reference point of the array is selected to coincide with its center of gravity. Therefore, the diagonal elements of the off-diagonal submatrices in (23) vanish

$$|k-k'| = nL, \quad n\in\{1,2,3,4\} \Longrightarrow F_{kk'}(\Omega)=0. \tag{26}$$

B. Special Case—Estimation of One Wave

It follows from (26) that $F(\Omega)$ is diagonal in the case $L=1$, so that analytic expressions for the CRLB's can easily be derived (see Appendix C)

$$\mathrm{CRLB}(\phi) = \frac{1}{\gamma_O}\,\frac{6}{\pi^2\sin^2(\phi)\,(M^2-1)} \tag{27}$$

$$\mathrm{CRLB}(\nu) = \frac{1}{\gamma_O}\,\frac{3}{2\pi^2 T_f^2(I^2-1)} \tag{28}$$

$$\mathrm{CRLB}(\tau) = \frac{1}{\gamma_O}\,\frac{1}{8\pi^2 B_u^2} \tag{29}$$

$$\begin{aligned}\mathrm{CRLB}\left(\frac{\alpha}{|\alpha|}\right) = \mathrm{CRLB}\left(\Re\left\{\frac{\alpha}{|\alpha|}\right\}\right) \\ + \mathrm{CRLB}\left(\Im\left\{\frac{\alpha}{|\alpha|}\right\}\right) = \frac{1}{\gamma_O}.\end{aligned} \tag{30}$$

The term $B_u \triangleq (1/\pi T_p)\sqrt{(N_s/2)\,(1+(1/K))}$ is the Gabor bandwidth[1] of $u(t)$. We have redefined $\tau \triangleq \tau_1$, $\phi \triangleq \phi_1$, $\nu \triangleq \nu_1$, and $\alpha \triangleq \alpha_1$. All CRLB's above are inversely proportional to $\gamma_O \triangleq MIKN_s\gamma_I$ which can be viewed as the signal-to-noise ratio (SNR) at the output of the correlator in Fig. 4. Notice that the SNR of the wave at the input of each antenna branch is $\gamma_I \triangleq P_u|\alpha|^2/(N_0/T_s)$. Both $\mathrm{CRLB}(\phi)$ and $\mathrm{CRLB}(\nu)$ depend on M and I in the same manner. Furthermore, $\mathrm{CRLB}(\phi)$ is inversely proportional to $\sin^2(\phi)$, i.e., a linear array is more sensitive to signals impinging nearby perpendicular to the array broadside. Increasing the interval T_f between two consecutive observations increases the temporal observation span and therefore decreases $\mathrm{CRLB}(\nu)$.

C. Special Case—Estimation of Two Waves with Equal Power

The resolution of conventional techniques for delay, azimuth, and Doppler frequency estimation like cross-correlation, Fourier, and beam-forming methods is limited

[1]The Gabor bandwidth of a signal is defined to be the root second central moment of its power spectrum [22]. Here, it is assumed to be finite.

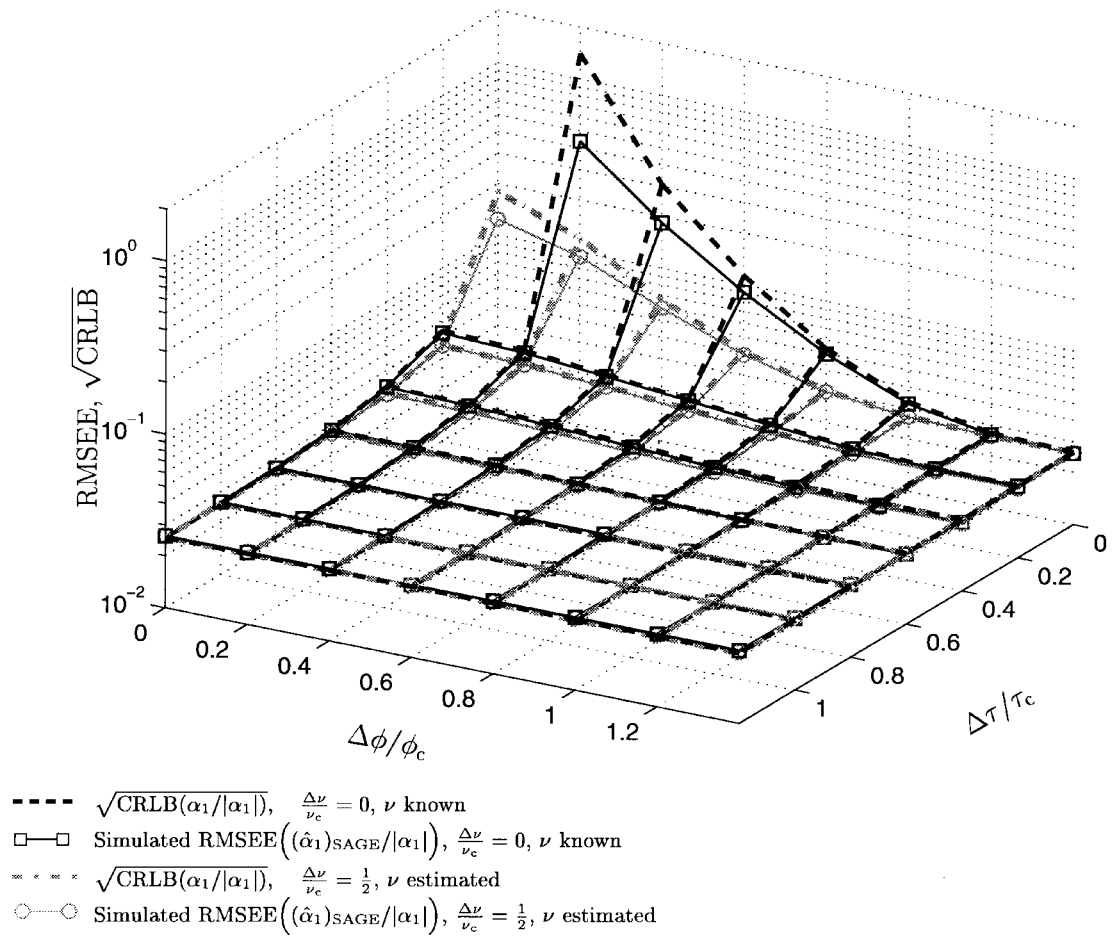

Fig. 6. $\sqrt{\text{CRLB}(\alpha_1/|\alpha_1|)}$ and RMSEE$((\hat{\alpha}_1)_{\text{SAGE}}/|\alpha_1|)$ as a function of $[\Delta\tau, \Delta\phi]$, with $\Delta\nu$ as a parameter.

by the intrinsic resolution of the measurement equipment. The resolution in delay, azimuth, and Doppler frequency is defined to be the half-width of the main lobe of the magnitude of the corresponding correlation function in (24). For a uniform linear array, these half-widths are given by

$$\tau_c = T_p, \quad \phi_c = \frac{360^\circ}{\pi M} \quad \text{and} \quad \nu_c = \frac{1}{IT_f} \tag{31}$$

respectively. The values of ϕ_c and ν_c are calculated for the broadside direction and for zero Doppler frequency, respectively. Two waves are called well separable or resolvable when the condition [21]

$$\Delta\tau > \tau_c \quad \text{or} \quad \Delta\phi > \phi_c \quad \text{or} \quad \Delta\nu > \nu_c \tag{32}$$

is satisfied.

The CRLB's result by inverting $F(\Omega)$ for $L = 2$. Each of these CRLB's are lower-bounded by the corresponding CRLB in (27)–(30), i.e., when each wave is considered separately [20]. Furthermore the former CRLB's are close to the latter when the two waves are well separable.

The following "two-wave" scenario is used as a basis for assessing the resolution ability of algorithms for wave parameter estimation: $L = 2$ waves with equal power are impinging at the Rx location with azimuths $\phi_1 = 90^\circ + (\Delta\phi/2)$ and $\phi_2 = 90^\circ - (\Delta\phi/2)$, respectively. The waves differ by the parameters $\Delta\phi$, $\Delta\tau \triangleq \tau_1 - \tau_2$, and $\Delta\nu \triangleq \nu_1 - \nu_2$. The complex amplitudes are selected as $\alpha_1 = -0.9511 - j0.3090$ and $\alpha_2 = 0.7431 + j0.6691$, respectively. Moreover it is assumed that the sounding sequence has unit power, i.e., $P_u = 1$ so that the SNR per wave at each antenna branch equals $\gamma_I = -20$ dB. The other parameters are set as described in Section V-D.

The square root of the CRLB's of the parameters of wave #1 has been evaluated numerically as a function of $\Delta\tau$, $\Delta\phi$, and $\Delta\nu$ for the above scenario. Two different situations have been investigated. In the first one the Doppler frequencies are known to be zero. As shown in Figs. 6 and 7 $\sqrt{\text{CRLB}(\alpha_1/|\alpha_1|)}$ and $\sqrt{\text{CRLB}(\phi_1)}$ significantly deviate from their lower bounds $\sqrt{\text{CRLB}(\alpha/|\alpha|)} = 0.025\,51$ and $\sqrt{\text{CRLB}(\phi)} = 0.104^\circ$, respectively, for $\Delta\tau < 0.2\tau_c$ and $\Delta\phi < \phi_c$. They remain below 0.3 and 0.7°, respectively, provided $\Delta\tau \geq 0.2\tau_c$ or $\Delta\phi \geq 0.4\phi_c$ and diverge toward infinity when $[\Delta\tau, \Delta\phi]$ tends to zero. In the second situation considered, the two waves exhibit distinct unknown Doppler frequencies. It appears from Figs. 6 and 7 that a difference of $\Delta\nu = \nu_c/2$ improves the resolution in delay and azimuth: In this case, we have $\sqrt{\text{CRLB}(\alpha_1)/|\alpha_1|} < 0.2$ and $\sqrt{\text{CRLB}(\phi_1)} < 0.21^\circ$ for any value of the pair $[\Delta\tau, \Delta\phi]$. It can be observed that as soon

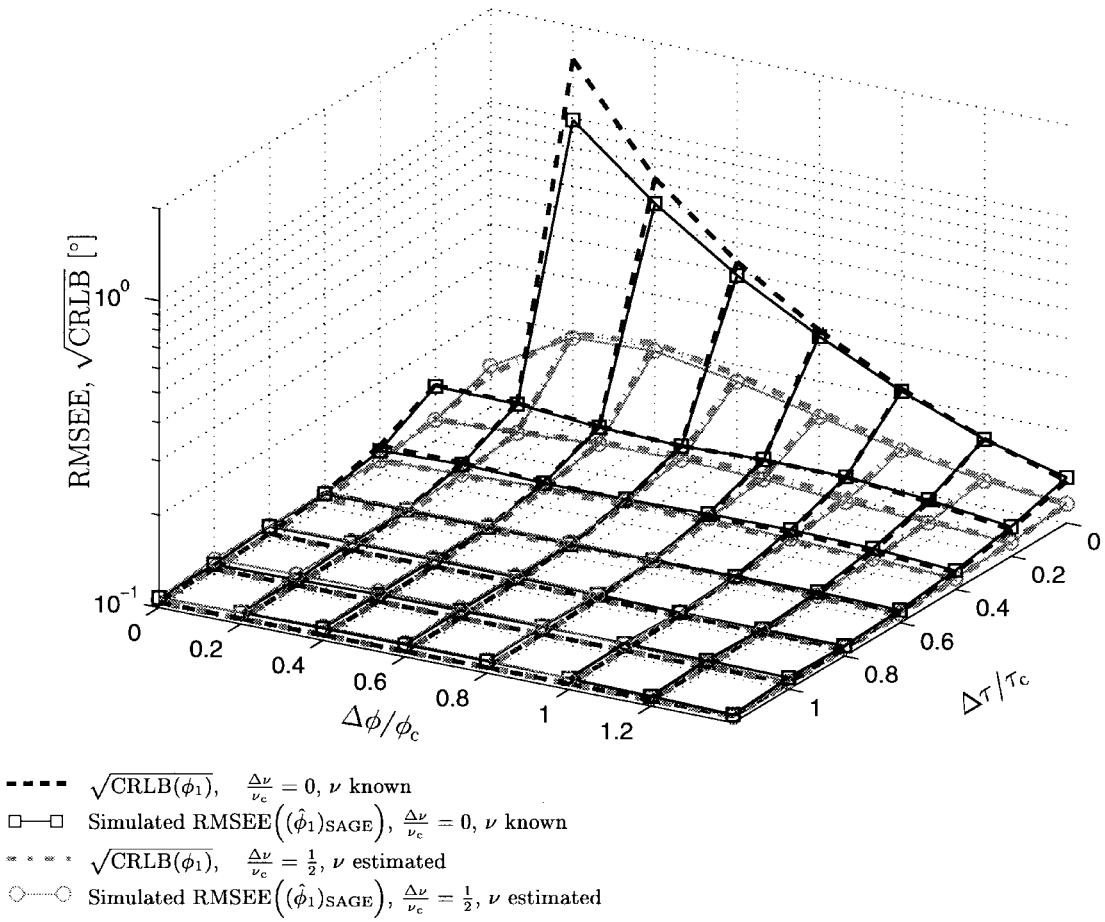

Fig. 7. $\sqrt{\text{CRLB}(\phi_1)}$ and RMSEE$((\hat{\phi}_1)_{\text{SAGE}})$ as a function of $[\Delta\tau, \Delta\phi]$, with $\Delta\nu$ as a parameter.

as $\Delta\tau \geq 0.4\tau_c$, the CRLB's are close to the corresponding CRLB's obtained in the single-wave scenario. This means that the waves can be resolved irrespectively of their separation in azimuth and Doppler frequency in this case. The CRLB's for α_1 and ϕ_1 as a function of $[\Delta\phi, \Delta\nu]$ are depicted in Figs. 8 and 9, respectively. Note that the maxima of $\sqrt{\text{CRLB}(\phi_1)}$ as a function of $\Delta\phi$ for fixed values $\Delta\tau$ (Fig. 7) or $\Delta\nu$ (Fig. 9) depend on the phase difference between α_1 and α_2.

D. RMSEE of the Parameter Estimates

The RMSEE's of the parameter estimates have been assessed by means of Monte Carlo simulations in the two situations described in Section V-C. We use a linear antenna array which comprises $M = 11$ equidistant elements with a spacing of $\lambda/2$. The pseudo-noise (PN) sounding sequence consists of $K = 127$ rectangular pulses $p(t)$ with $T_p = 10$ ns. Hence, $T_a = 1.27$ μs. The parameter estimates are quantized to a precision of $\tau_c/10 = T_p/10 = 1$ ns, $\phi_c/500 = 0.0208°$, and $\nu_c/500 = 0.1632$ Hz, respectively. The parameter estimates are initialized by applying the successive cancellation scheme. After the initialization, which is labeled as the zeroth cycle, the scheme performs 100 iteration cycles.

The RMSEE's of $(\hat{\alpha}_1)_{\text{SAGE}}/|\alpha_1|$ and $(\hat{\phi}_1)_{\text{SAGE}}$ are shown in Figs. 6–9. While the RMSEE's are close to $\sqrt{\text{CRLB}}$ for well resolvable waves, they deviate significantly from the latter when the triple $[\Delta\tau, \Delta\phi, \Delta\nu]$ lies in a certain domain around zero. Further simulation results not being reported here indicate that the parameter estimates are biased which, in view of (21), leads to the aforementioned deviation. These simulations also reveal that when the wave separation is decreased the bias can be compensated for by decreasing the quantization precision of the parameter estimates. From Figs. 6–9 we can conclude that if either $\Delta\nu \gtrapprox \nu_c/2$, or $\Delta\phi \gtrapprox \phi_c/2$, or $\Delta\tau \gtrapprox \tau_c/5$, the RMSEE's are close to the values of $\sqrt{\text{CRLB}}$ for the single-wave scenario and, consequently, that the waves are resolvable.

The convergence rate of the SAGE algorithm is illustrated in Figs. 10 and 11, where the transient behavior of the RMSEE's is reported for the two investigated situations. Varying $[\Delta\tau, \Delta\phi]$ on the line $\Delta\tau/\tau_c + \Delta\phi/\phi_c = 0.4$, we observe that the convergence rate increases for decreasing values of $\Delta\phi$ due to the simultaneous increase of $\Delta\tau$. The rate increase is pronounced for increasing values of $\Delta\nu$. As can be seen from the figures, for resolvable waves the RMSEE's of the parameter estimates approach $\sqrt{\text{CLRB}}$ after roughly 20 iteration cycles. In this case the two waves are easily resolvable in the sense that the required effort to compute the estimates with an accuracy close to the corresponding CRLB is low. Some RMSEE sequences are observed to converge to a value lower than the corresponding $\sqrt{\text{CRLB}}$. This behavior results when the estimates are significantly biased for the reason mentioned in the previous paragraph.

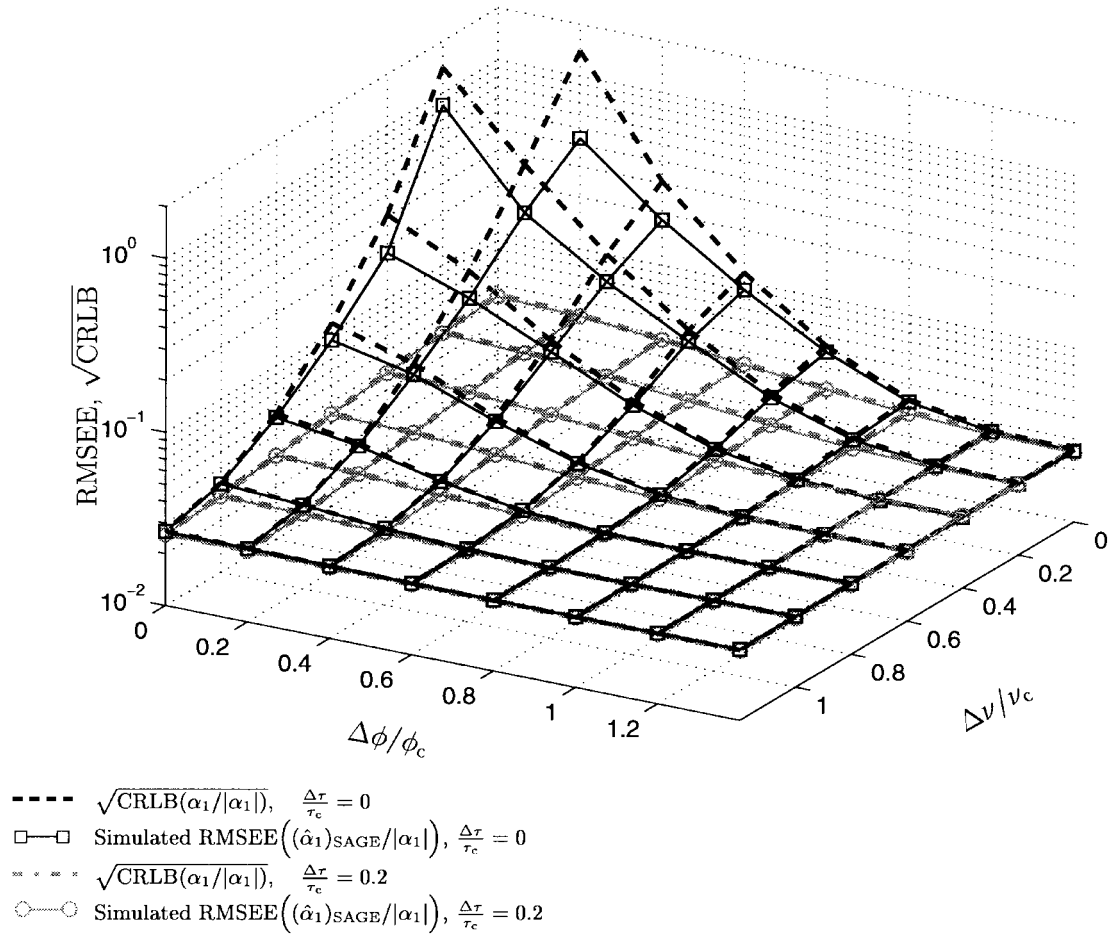

Fig. 8. $\sqrt{\text{CRLB}(\alpha_1/|\alpha_1|)}$ and RMSEE$((\hat{\alpha}_1)_{\text{SAGE}}/|\alpha_1|)$ as a function of $[\Delta\phi, \Delta\nu]$, with $\Delta\tau$ as a parameter.

VI. Performance in Real Channels

A. Performance Criteria

The performance of the SAGE algorithm has also been tested in real conditions by applying it to data obtained during various measurement campaigns in pico- and macro-cellular environments. It is a nontrivial task to verify whether the SAGE algorithm actually returns correct channel estimates in such a situation because the real channel is unknown and the underlying model assumption that specular plane waves are impinging at the Rx does not usually hold.

Three different criteria are proposed to evaluate the performance of the SAGE algorithm in real channels [11].

- First, the power delay and azimuth profiles are computed from the actual signals measured at the output of the antenna branches. The power azimuth profile is calculated by using the conventional beam-forming method [23] while the power delay profile is obtained by averaging the squared magnitude of the signals correlator/matched filter output. Second, the same profiles are recalculated using $s(t;\hat{\theta}_{\text{SAGE}})$. Notice that all of these profiles embody the delay or azimuth response of the measurement setup. A comparison of the measurement- and reconstruction-based profiles allows an indirect verification whether the scheme returns meaningful channel estimates.
- An alternative criterion for assessing the accuracy of the SAGE algorithm is to relate the waves estimated by means of the scheme to some scatterers in the investigated propagation environment. Based on the estimates of the delay, azimuth, and Doppler frequency of an impinging wave, we can reconstruct its path between the Tx and the Rx while assuming single scattering/reflection in the propagation environment. The applicability of this method is limited, however, as experimental evidence indicates that a nonnegligible part of the impinging waves reaches the Rx by means of multiple scattering/reflection.
- The convergence rate of the SAGE algorithm as well as the number of iteration cycles required until the scheme has converged are assessed by monitoring the sequence of log-likelihood values $\{\Lambda(\hat{\theta}(\mu);y)\}$.

B. Time-Invariant Channels

The first measurement campaign was conducted in a pico-cellular environment by using the wide-band channel sounder developed at the Communication Technology Laboratory of the Swiss Federal Institute of Technology, Zurich [24]. The equipment transmits a carrier at the frequency of 1.98 GHz modulated with a PN sequence of period $K = 255$. The chip duration is $T_p = 10$ ns so that $T_a = KT_p = 2.55$ μs.

The measurements were performed in a courtyard of size 9 m $\times$ 17 m located inside a building (see Fig. 12). Both Tx and

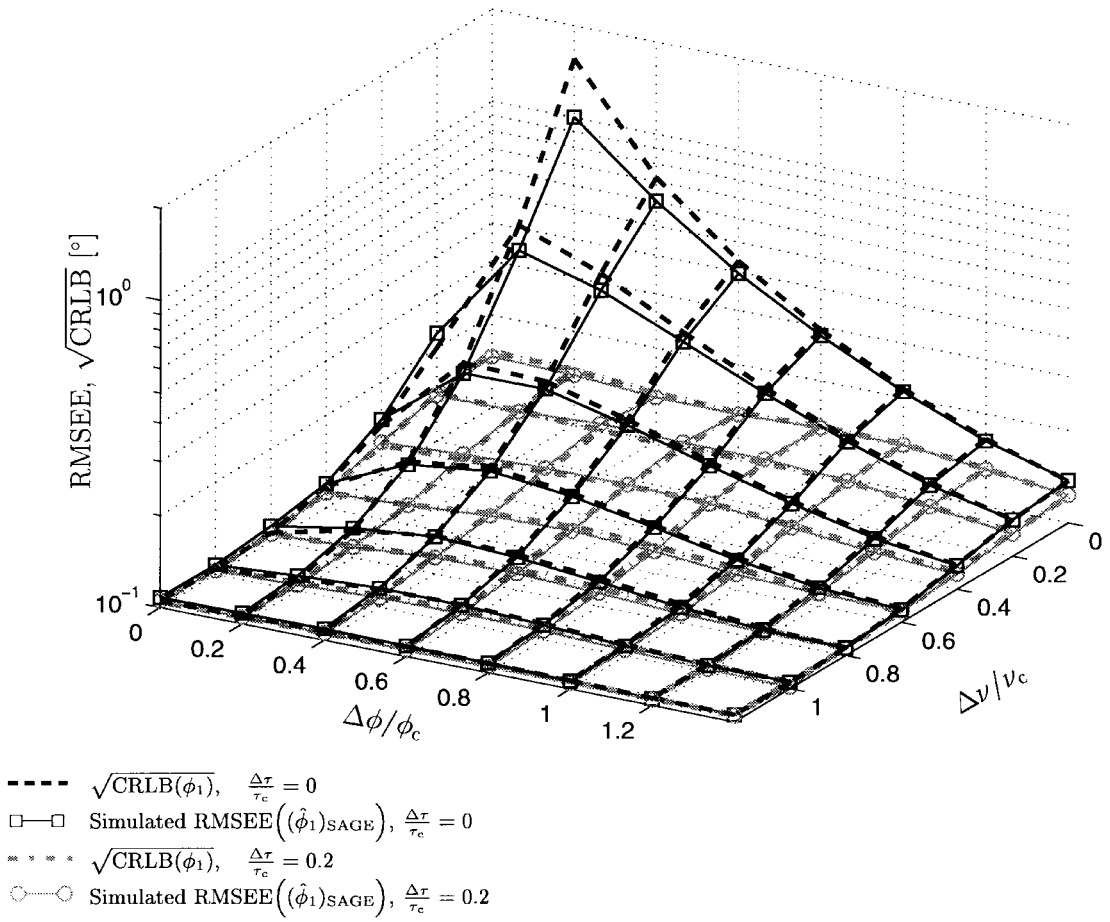

Fig. 9. $\sqrt{\text{CRLB}(\phi_1)}$ and RMSEE$((\hat{\phi}_1)_{\text{SAGE}})$ as a function of $[\Delta\phi, \Delta\nu]$, with $\Delta\tau$ as a parameter.

Rx were fixed, and no object was moving in the surroundings so that the environment is time-invariant. A line-of-sight (LOS) path exists between the Tx and the Rx which are located 9.8 m apart from each other. The signal at the correlator output of the Rx has been recorded at ten locations on a circle and at its center. The distance between two neighboring locations on the circle is 0.5λ. The 11 recorded signals are identified with those present at the output of a correlator bank connected to a virtual antenna array with $M = 11$ sensors located at the measurement positions. The selected array geometry allows an unambiguous azimuth estimation in the full range [0°, 360°). An industrial robot has been used to place the receiving antenna at the desired locations. The quantization precision of the SAGE algorithm is 1 ns and 0.05°. The number of waves to be estimated is set to $L = 20$. The received signal is observed over $I = 1$ period. The initialization is performed by means of the successive cancellation scheme described in Section IV-B.

The estimated delay-azimuth spread function of the channel [25] is depicted in Fig. 13. This function is defined to be $\hat{h}(\tau, \phi) \triangleq \Sigma_{\ell=1}^{L} \hat{\alpha}_\ell \delta(\tau - \hat{\tau}_\ell)\delta(\phi - \hat{\phi}_\ell)$, where $\delta(\cdot)$ denotes the Dirac distribution. In addition to the LOS wave, three other waves can be related to a reflector/scatterer from which they originate. Table I contains the estimated parameter values of the four waves as well as the corresponding delay difference $\hat{\tau}_{\ell\,\text{calc}}$ calculated from the reconstructed paths in Fig. 12. Notice that $\ell = 1$ is the index of the wave propagating along the LOS path and we have set $\hat{\tau}_{1,\text{calc}} \triangleq \hat{\tau}_1$. The relative delay errors $|(\hat{\tau}_\ell - \hat{\tau}_{\ell\,\text{calc}})/(\hat{\tau}_\ell - \hat{\tau}_1)|$, $\ell \in \{2, \ldots, 4\}$, range from 9–16%. The cause of the large deviations could not be definitely identified. The other waves estimated by the SAGE algorithm could not be related to the environment. Their azimuth is spread homogeneously over [0°, 360°). Considering the estimated delays, some of the waves probably originate from reflectors/scatterers located inside the building situated to the left of the yard. These waves experience little attenuation when they propagate through the large windows in the wall fronting the yard.

C. Time-Variant Channels

The second measurement campaign was conducted by using the stand-alone testbed developed within the TSUNAMI II project at the Center for PersonKommunikation, Aalborg University [26]. The testbed consists of a receiving base station (BS) equipped with an eight-element phased antenna array and a transmitting mobile station (MS) equipped with an omni-directional antenna. It is designed according to the DCS1800 (Digital Cellular System 1800) standard [27] and is implemented for up-link only. The eight signals at the array output are sampled at the rate $1/T_s$, with $T_s = 0.923$ μs, and stored on a hard disk for every TDMA-frame, i.e., $T_f = 4.6$ ms, for off-line processing. The measurement campaign was conducted in downtown Aalborg, Denmark, with the MS and BS located as illustrated in Fig. 14.

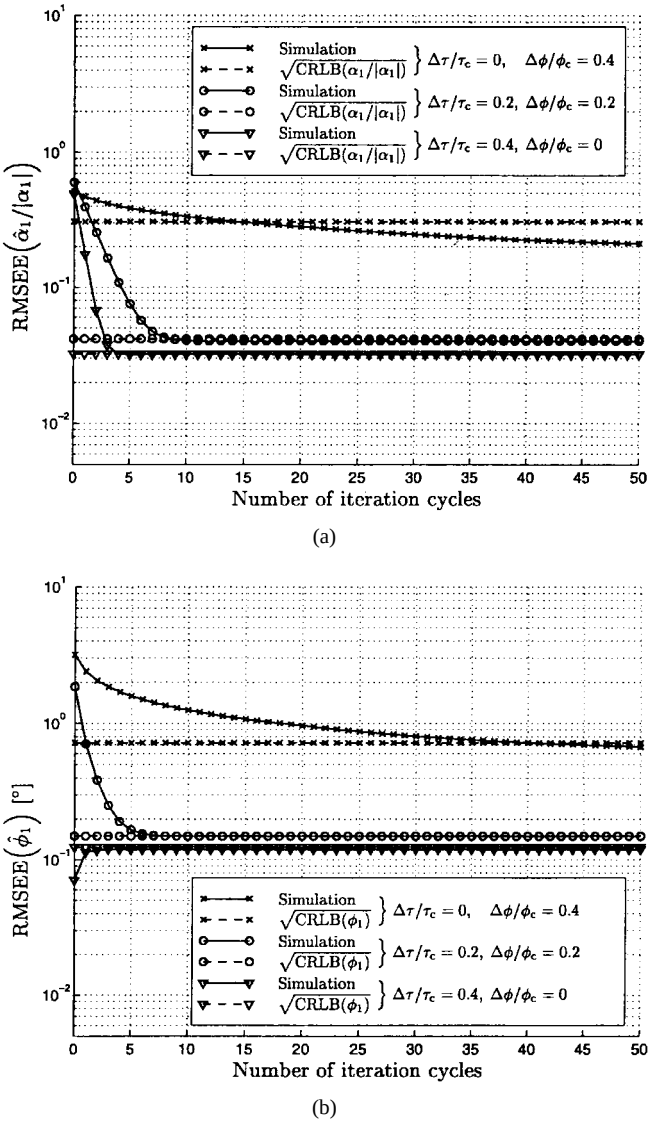

Fig. 10. (a) RMSEE$(\hat{\alpha}_1/|\alpha_1|)$ and (b) RMSEE$(\hat{\phi}_1)$ versus the number of iteration cycles for different values of $[\Delta\tau, \Delta\phi]$ and $\Delta\nu = 0$.

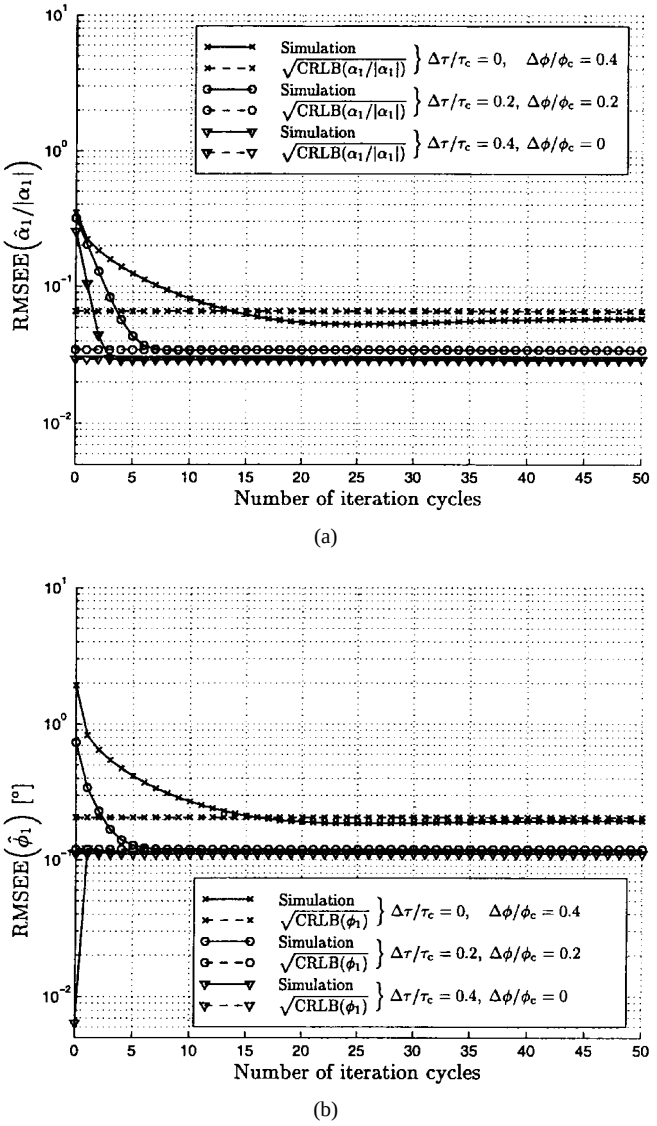

Fig. 11. (a) RMSEE$(\hat{\alpha}_1/|\alpha_1|)$ and (b) RMSEE$(\hat{\phi}_1)$ versus the number of iteration cycles for different values of $[\Delta\tau, \Delta\phi]$ and $\Delta\nu/\nu_c = 0.5$.

An example of the estimated azimuth-Doppler spread function $\hat{h}(\phi,\nu) \triangleq \Sigma_{\ell=1}^{L}\ \hat{\alpha}_\ell\delta(\phi-\hat{\phi}_\ell)\delta(\nu-\hat{\nu}_\ell)$ and delay-azimuth spread function is shown in Fig. 15. In this particular situation the azimuth toward the Tx was 22°. It is observed that most of the received power arrives from that direction, so that the angular spread of the channel is relatively small. This observation is consistent with previous experimental results reported in [28] and [29] which show that the angular spread is usually less than 5°. As predicted by the simulation results reported in Section V, the SAGE algorithm is capable of resolving the waves with almost identical azimuths as long a their Doppler frequencies or relative delays differ sufficiently. As shown in Fig. 1 the Doppler frequency of a wave impinging on the BS depends on the azimuth between the direction of movement and the first object with which the wave interacts. The same figure points out that many waves with distinct Doppler frequencies might be impinging on the BS from two nearby directions which cannot be distinguished from each other.

It is quite difficult to relate most of the individual components among the cluster around 22° to an object in the environment. The strong wave with azimuth 20°, delay $6T_s$, and Doppler frequency 0 Hz, originates from a reflection on a large building front (see Fig. 14). The SAGE algorithm does also detect a few impinging waves at approximately −20°. The one with delay equal to $6T_s$ is a reflection from a high hotel building. The azimuth and delay profiles obtained from the measured and reconstructed array out signals is reported in Fig. 16. There is a good match between both types of profiles for signal components higher than −20 dB. Below −20 dB the fit is less accurate due to receiver noise as well as model imperfections in the reproduction of the response of the measurement system.

The convergence behavior of the SAGE algorithm is illustrated in Fig. 17 for some measurements in both types of investigated environments. Each sequence $\{\Lambda(\hat{\theta}(\mu); y)\}$ is normalized by $\Lambda(\hat{\theta}(20); y\}$. The latter figure provides an estimate of the limit toward which the sequence converges.

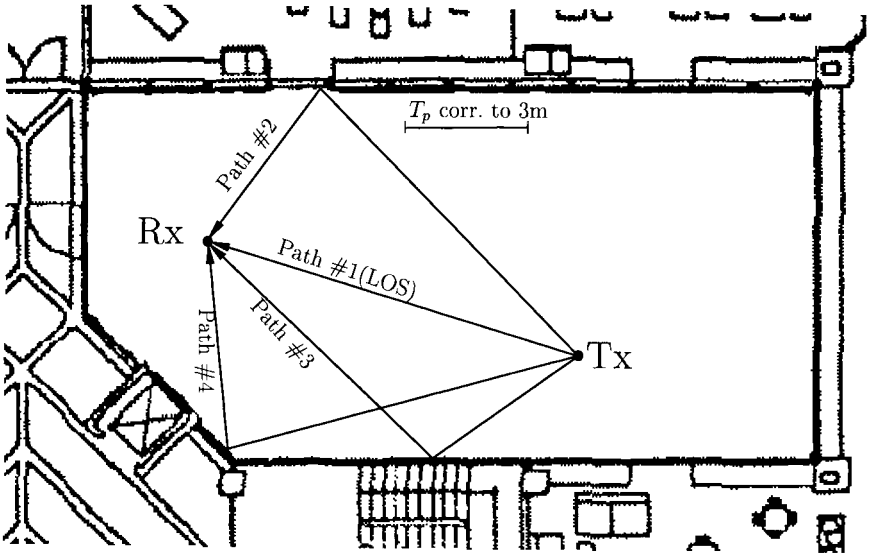

Fig. 12. Map of the premises of the pico-cellular location including the path of the waves which can be related to scatterers/reflectors.

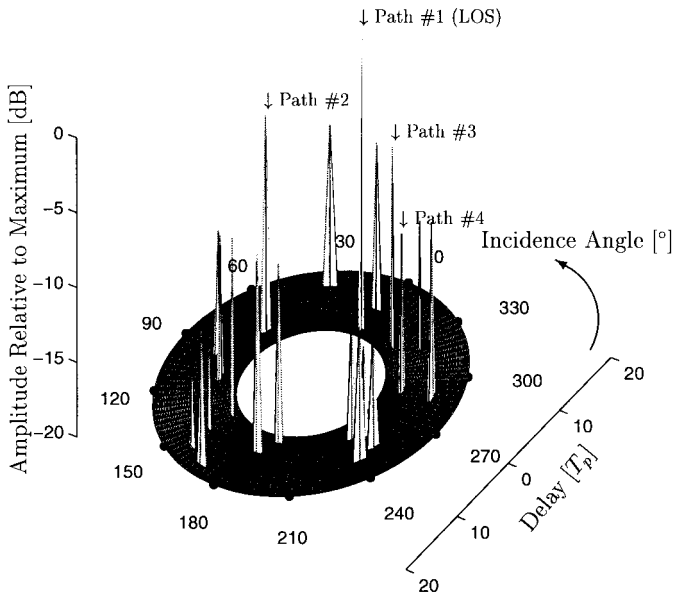

Fig. 13. Estimated delay-azimuth spread function obtained in the pico-cellular environment $(L = 20)$.

TABLE I
INCIDENCE PARAMETERS OF THE WAVE WHICH CAN BE RELATED WITH THE PROPAGATION ENVIRONMENT IN FIG. 12

ℓ	relative power [dB]	$(\hat{\tau}_\ell - \hat{\tau}_1)$ $[T_p]$	$(\hat{\tau}_{\ell\text{calc}} - \hat{\tau}_{1\text{calc}})$ $[T_p]$	$\left(\hat{\phi}_\ell - \hat{\phi}_1\right)$ [°]
1 (LOS)	0	0	0	0
2	-5.6	1.6	1.34	66.6
3	-6.7	0.8	0.73	334.25
4	-9.5	1.3	1.46	292.75

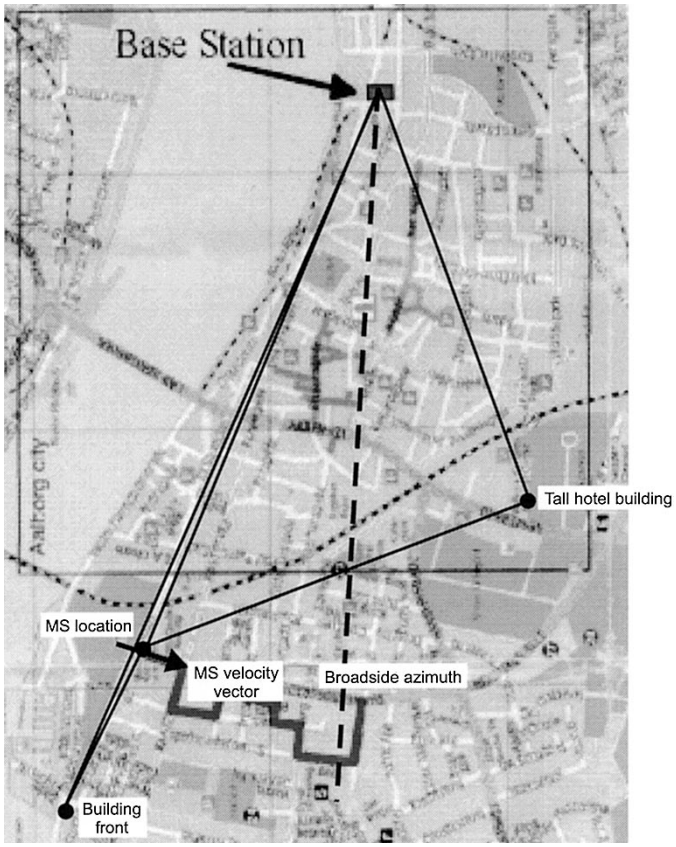

Fig. 14. Map of central Aalborg. The thick broken line denotes the route of the MS.

The log-likelihood sequences significantly increase within the first iteration cycles and have almost converged after ten iteration cycles.

The value of $\Lambda(\hat{\theta}(0); y)/\Lambda(\hat{\theta}(20); y)$ is larger when the successive cancellation scheme is used. This might be explained by the fact that the cancellation of already estimated waves in the received signal $y(t)$ increases the accuracy with which the remaining waves can be estimated. Nevertheless, the convergence rate of the sequences is almost identical after one iteration cycle regardless of the initialization procedure. This behavior indicates that the SAGE algorithm exhibits some robustness against the initialization methods. The convergence

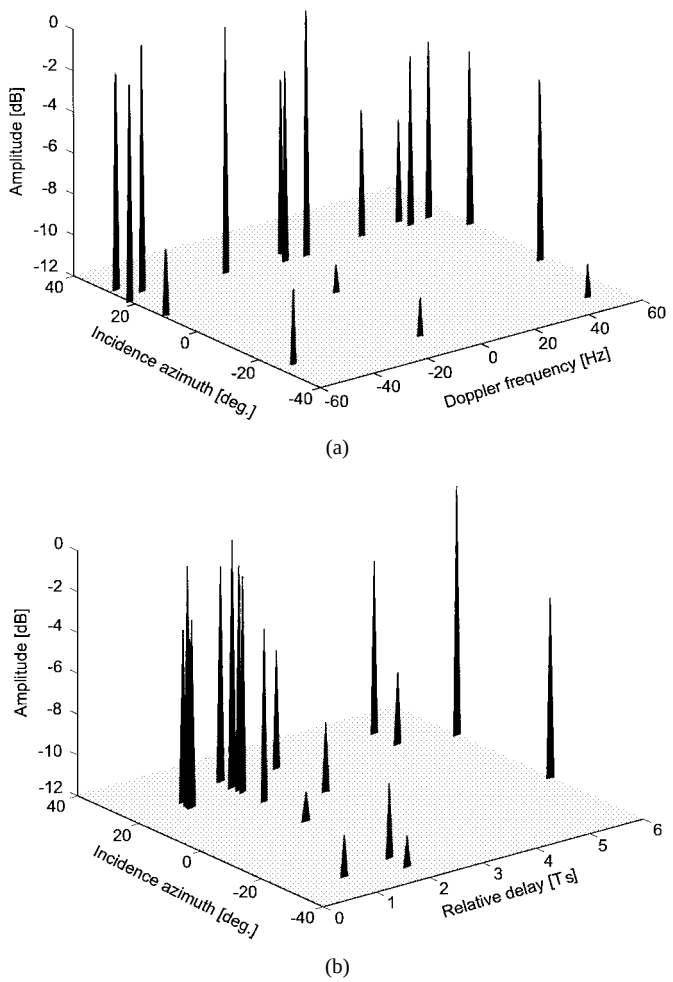

Fig. 15. (a) Example of an estimated azimuth-Doppler spread function and (b) an estimated delay-azimuth spread function in a macro-cellular environment ($T_s = 0.923$ μs).

rate of the SAGE algorithm is slightly slower when it is applied to measurement data than when it is used with synthetic data. This behavior is also expected since, in real environments, the impinging waves might embody a diffusely scattered component so that the underlying model assumption of specular incident waves does not hold.

VII. Conclusions

The performance of the SAGE algorithm applied for separating impinging waves with respect to their relative delay, incidence azimuth, and Doppler frequency in mobile radio environments has been investigated in synthetic and real conditions. Monte Carlo simulations in synthetic environments demonstrate the high resolution ability of the scheme: it is capable of easily separating waves as soon as one of their three parameters differ by more than roughly half the intrinsic resolution of the measurement equipment. Two waves are assumed to be separated when the MSEE's of their parameter estimates are close to the corresponding CRLB's obtained when each wave is considered separately. The term easily means that the SAGE algorithm converges rapidly, i.e., within less than 20 iteration cycles. Convergence is meant to be achieved when the MSEE's approach the corresponding CRLB's.

When the SAGE algorithm is used in real environments, the log-likelihood sequence essentially converges within ten iteration cycles. Various validation techniques indicate that the SAGE algorithm returns consistent estimates.

Due to its appealing properties, the SAGE algorithm proves to be a powerful tool for off-line processing of extensive channel measurement data especially for channel modeling purposes [30], [11]. The presented experimental results show in particular that it can be successfully applied to resolve waves with arbitrarily close incidence azimuths, a situation frequently encountered at the base stations in macro-cellular environments. Other studies have revealed that the SAGE algorithm is also a promising candidate for channel estimation in direct-sequence code-division multiple access communication systems [31]–[33].

Appendix A
Derivation of (22)

We start with the log-likelihood function (4) for the given estimation problem, where we have replaced θ by its real-valued version Ω defined in (18). The elements of the FIM are defined as $F_{kk'}(\Omega) = -\boldsymbol{E}_\Omega[(\partial/\partial\Omega_k)\,(\partial/\partial\Omega_{k'})\Lambda(\Omega;Y)]$, $k,k' = 1,\ldots,5L$, [34], [35]. Using the identity $2\Re(a^{\mathrm{H}}b) = a^{\mathrm{H}}b + b^{\mathrm{H}}a$ in (4), the second order derivative in the previous expectation is given by

$$\begin{aligned}\frac{\partial}{\partial\Omega_k}\,\frac{\partial}{\partial\Omega_{k'}}\Lambda(\Omega;y) &= \frac{1}{N_0}\left[\int_{D_o}\frac{\partial}{\partial\Omega_k}\,\frac{\partial}{\partial\Omega_{k'}}s^{\mathrm{H}}(t';\Omega)\,(y(t')-s(t';\Omega))\,dt'\right.\\ &\quad+\int_{D_o}(y(t')-s(t';\Omega))^{\mathrm{H}}\,\frac{\partial}{\partial\Omega_k}\,\frac{\partial}{\partial\Omega_{k'}}s(t';\Omega)\,dt'\\ &\quad-\int_{D_o}\frac{\partial}{\partial\Omega_k}s^{\mathrm{H}}(t';\Omega)\,\frac{\partial}{\partial\Omega_{k'}}s(t';\Omega)\,dt'\\ &\quad\left.-\int_{D_o}\frac{\partial}{\partial\Omega_{k'}}s^{\mathrm{H}}(t';\Omega)\,\frac{\partial}{\partial\Omega_k}s(t';\Omega)\,dt'\right].\end{aligned}$$

Equation (22) follows immediately by applying again the above identity to the last two terms and by noting that the expectation of the first two terms vanish because of $\boldsymbol{E}_\Omega[Y(t)-s(t;\Omega)] = 0$.

Appendix B
Derivation of (25)

Let us define $m(t;\Omega) \triangleq [s^{\mathrm{T}}(t-((I-1)/2)T_f;\Omega),\, s^{\mathrm{T}}(t-((I-3)/2)T_f;\Omega),\ldots,s^{\mathrm{T}}(t+((I-1)/2)T_f;\Omega)]^{\mathrm{T}}$. Equation (22) can then be rewritten according to

$$F_{kk'}(\Omega) = \frac{2}{N_0}\Re\left\{\int_{-T_a/2}^{T_a/2}\frac{\partial}{\partial\Omega_k}m^{\mathrm{H}}(t';\Omega)\cdot\frac{\partial}{\partial\Omega_{k'}}m(t';\Omega)dt'\right\}. \tag{33}$$

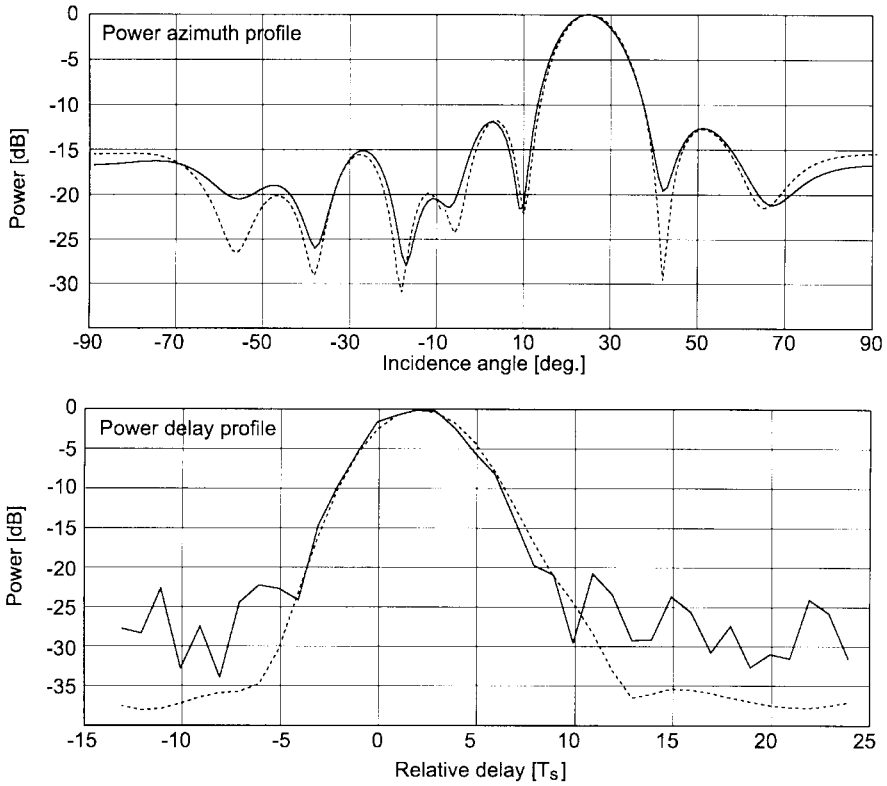

Fig. 16. Power azimuth and delay profiles computed from the measured (solid) and the reconstructed (dashed) signals at the array output.

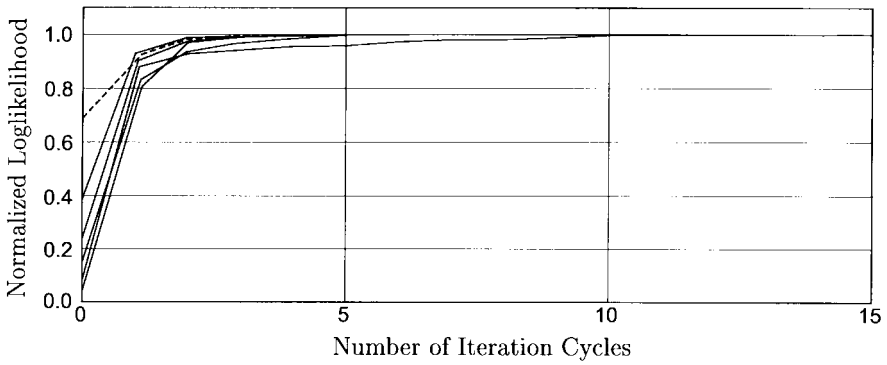

Fig. 17. Loglikelihood values versus the number of iteration cycles for different measurement data: pico-cellular environment (dashed), macro-cellular environments (solid).

The MI-D vector-valued function $m(t;\Omega)$ can be expressed in the compact notation

$$m(t;\Omega) = \sum_{\ell=1}^{L} \alpha_\ell u(t-\tau_\ell) d(\nu_\ell) \otimes c(\phi_\ell) \tag{34}$$

where $\otimes$ denotes the Kronecker product. Notice that we also make use of (1) and (3) to obtain (34). Then, (25) results by inserting (34) in (33) and invoking the identities $(a \otimes b)^{\mathrm{H}} = a^{\mathrm{H}} \otimes b^{\mathrm{H}}$ and $(a_1 \otimes b_1)^{\mathrm{H}}(a_2 \otimes b_2) = (a_1^{\mathrm{H}} a_2) \otimes (b_1^{\mathrm{H}} b_1)$.

Appendix C
Derivation of the CRLB's in (27)–(30)

In the case $L = 1$, it follows from (26) that all nondiagonal elements of the FIM vanish. Hence, $\mathrm{CRLB}(\Omega_k)$ is obtained by inverting the element $F_{kk}(\Omega)$ of $F(\Omega)$. We first derive $\mathrm{CRLB}(\nu)$ in (28). The proof is analogous to that given in [36] for $\mathrm{CRLB}(\phi)$. It can be easily shown from (25) that the components of the submatrix $F_{\nu\nu}(\Omega)$ in (23) are given by

$$(F_{\nu\nu})_{\ell\ell'}(\Omega) = 2\gamma \Re\left\{ \alpha_\ell^* \alpha_{\ell'} \rho(\tau_\ell - \tau_{\ell'}) \zeta(\phi_\ell, \phi_{\ell'}) \cdot \frac{\partial}{\partial \nu_\ell} \frac{\partial}{\partial \nu_{\ell'}} \eta(\nu_\ell, \nu_{\ell'}) \right\}. \tag{35}$$

For the case $L = 1$, we have $\ell = \ell' = 1$ so that (35) reduces to

$$\begin{aligned}(F_{\nu\nu})_{1,1}(\Omega) &= 2\gamma|\alpha|^2 \Re\left\{ \frac{\partial}{\partial \nu} \frac{\partial}{\partial \nu'} \eta(\nu,\nu') \Big|_{\nu=\nu'} \right\} \\ &= \frac{2\gamma|\alpha|^2}{I} \Re\left\{ \sum_{i=1}^{I} \left| \frac{\partial}{\partial \nu} d_i(\nu) \right|^2 \right\} \\ &= \frac{\gamma|\alpha|^2 8\pi^2 T_f^2}{I} \sum_{i=1}^{I} \left(i - \frac{I+1}{2} \right)^2 \\ &= \frac{2}{3}\, \gamma_O \pi^2 T_f^2 (I^2 - 1).\end{aligned}$$

The last term results from the identity $\Sigma_{i=1}^{I} i^2 = I(I+1)(2I+1)/6$ and noting that $\gamma_O = |\alpha|^2\gamma$.

Invoking (25) again, we can show that the components of the submatrix $(F_{\tau\tau})_{\ell\ell'}(\Omega)$ take the form

$$(F_{\tau\tau})_{\ell\ell'}(\Omega) = 2\gamma\Re\left\{\alpha_\ell^*\alpha_{\ell'}\,\frac{\partial}{\partial\tau_\ell}\,\frac{\partial}{\partial\tau_{\ell'}}\rho(\tau_\ell-\tau_{\ell'}) \cdot\zeta(\phi_\ell,\phi_{\ell'})\eta(\nu_\ell,\nu_{\ell'})\right\}. \tag{36}$$

Identity (29) follows from (36) and $(d^2/d\tau^2)\rho(\tau)|_{\tau=0} = -(2\pi B_u)^2$, where B_u is the Gabor bandwidth [22] of $u(t)$. The proof of (30) is trivial.

ACKNOWLEDGMENT

The authors would like to thank Dr. P. E. Mogensen for providing the time-variant channel measurements and for many useful discussions during the work. Also, the effort of laboratory engineers F. Frederiksen, K. Olesen, and S. Larsen for building the TSUNAMI II testbed and conducting the measurements is appreciated. Finally, they express their gratitude to G. Furia from the Computer Integrated Manufacturing (CIM) Center, Manno (Switzerland) for providing the robot as well as the related technical support during the measurement campaign conducted in the pico-cellular environment.

REFERENCES

[1] H. Krim and M. Viberg, "Two decades of array signal processing research," *IEEE Signal Processing Mag.*, pp. 67–94, July 1996.
[2] R. O. Schmidt, "Multiple emitter location and signal parameter estimation," *IEEE Trans. Antennas Propagat.*, vol. AP-34, pp. 276–280, Mar. 1986.
[3] R. Roy and T. Kailath, "ESPRIT—Estimation of signal parameters via rotational invariance techniques," *IEEE Trans. Acoust., Speech, Signal Processing*, vol. 37, pp. 984–995, July 1989.
[4] M. Haardt and J. Nossek, "Unitary ESPRIT: How to obtain increased estimation accuracy with a reduced computational burden," *IEEE Trans. Signal Processing*, vol. SP-43, pp. 1232–1242, May 1995.
[5] T. Lo, J. Litva, and H. Leung, "A new approach for estimating indoor radio propagation characteristics," *IEEE Trans. Antennas Propagat.*, vol. 42, no. 10, pp. 1369–1376, 1994.
[6] A. van der Veen, M. Vanderveen, and A. Paulraj, "Joint angle and delay estimation using shift-invariance properties," *IEEE Signal Processing Lett.*, vol. 4, pp. 142–145, May 1997.
[7] M. Zoltowski, M. Haardt, and C. Mathews, "Closed-form 2-D angle estimation with rectangular arrays in element space or beamspace via unitary ESPRIT," *IEEE Trans. Signal Processing*, vol. SP-44, pp. 316–328, Feb. 1996.
[8] J. Fuhl, J.-P. Rossi, and E. Bonek, "High-resolution 3-D direction-of-arrival determination for urban mobile radio," *IEEE Trans. Antennas Propagat.*, vol. AP-45, pp. 672–682, Apr. 1997.
[9] M. Feder and E. Weinstein, "Parameter estimation of superimposed signals using the EM algorithm," *IEEE Trans. Acoust., Speech, Signal Processing*, vol. 36, pp. 477–489, Apr. 1988.
[10] B. H. Fleury, D. Dahlhaus, R. Heddergott, and M. Tschudin, "Wideband angle of arrival estimation using the SAGE algorithm," in *Proc. IEEE Fourth Int. Symp. Spread Spectrum Techniques and Applications (ISSSTA '96)*, Mainz, Germany, Sept. 1996, pp. 79–85.
[11] K. Pedersen, B. Fleury, and P. Mogensen, "High resolution of electromagnetic waves in time-varying radio channels," in *Proc. 8th IEEE Int. Symp. Personal, Indoor and Mobile Radio Communications (PIMRC '97)*, Helsinki, Finland, Sept. 1997.
[12] M. Tschudin, R. Heddergott, and P. Truffer, "Validation of a high resolution measurement technique for estimating the parameters of impinging waves in indoor environments," in *Proc. 9th IEEE Int. Symp. Personal, Indoor and Mobile Radio Communications (PIMRC '98)*, Boston, MA, Sept. 1998, pp. 1411–1416.
[13] M. Wax and T. Kailath, "Detection of signals by information theoretic criteria," *IEEE Trans. Acoust., Speech, Signal Processing*, vol. ASSP-33, pp. 387–392, Apr. 1985.
[14] H. V. Poor, *An Introduction to Signal Detection and Estimation*. New York: Springer-Verlag, 1988.
[15] G. McLachlan and T. Krishnan, *The EM Algorithm and Extensions. Probability and Statistics*. New York: Wiley, 1996.
[16] T. Moon, "The expectation-maximization algorithm," *IEEE Signal Processing Mag.*, 1997, pp. 47–60.
[17] A. P. Dempster, N. M. Laird, and D. B. Rubin, "Maximum likelihood from incomplete data via the EM algorith," *J. Royal Statist. Soc., Ser. B*, vol. 39, no. 1, pp. 1–38, 1977.
[18] J. M. Wozencraft and I. M. Jacobs, *Principles of Communication Engineering*. New York: Wiley, 1965.
[19] J. A. Fessler and A. O. Hero, "Space-alternating generalized expectation-maximization algorithm," *IEEE Trans. Signal Processing*, vol. 42, pp. 2664–2677, Oct. 1994.
[20] E. L. Lehmann, *Theory of Point Estimation*. New York: Wiley, 1983.
[21] D. H. Johnson and D. E. Dudgeon, *Array Signal Processing: Concepts and Techniques*. Englewood Cliffs, NJ: Prentice-Hall, 1993.
[22] F. Amoroso, "The bandwidth of digital data signals," *IEEE Commun. Mag.*, pp. 13–24, Nov. 1980.
[23] B. D. Veen and K. M. Buckley, "Beamforming: A versatile approach to spatial filtering," *IEEE ASSP Magazine*, pp. 4–24, Apr. 1988.
[24] E. Zollinger, "Eigenschaften von Funkübertragungsstrecken in Gebäuden," Ph.D. dissertation, ETH no. 10064, Swiss Federal Institute of Technology, Zurich, 1993.
[25] B. H. Fleury and P. E. Leuthold, "Radiowave propagation in mobile communications: An overview of European research," *IEEE Commun. Mag.*, vol. 34, pp. 70–81, Feb. 1996.
[26] P. Mogensen, F. Frederiksen, H. Dam, K. Olesen, and S. Larsen, "Tsunami (II) stand alone testbed," in *Proc. ACTS Mobile Communications Summit*, Granada, Spain, 1996, pp. 517–527.
[27] "GSM05.05 European Digital Cellular Telecommunications Systems-Modulation, Version 4.10.0," European Telecommunications Standards Institute (ETSI), Tech. Rep., 1992.
[28] P. Eggers, "Angular-temporal domain analogies of the short-term mobile radio propagation channel at the base station," in *Proc. 7th IEEE Int. Symp. Personal, Indoor and Mobile Radio Communications (PIMRC '96)*, May 1996, pp. 742–746.
[29] P. E. Mogensen, K. I. Pedersen, P. Leth-Espensen, B. Fleury, F. Frederiksen, K. Olesen, and S. L. Larsen, "Preliminary measurement results from an adaptive antenna array testbed for GSM/UMTS," in *Proc. IEEE Vehicular Technology Conference (VTC '97)*, Phoenix, AZ, 1997, pp. 1592–1596.
[30] K. I. Pedersen, P. E. Mogensen, and B. H. Fleury, "Power azimuth spectrum in outdoor environments," *Electron. Lett.*, vol. 33, pp. 1583–1584, Aug. 28, 1997.
[31] M. Feder and J. A. Catipović, "Algorithms for joint channel estimation and data recovery—Application to equalization in underwater communications," *IEEE J. Oceanic Eng.*, vol. 16, pp. 42–55, Jan. 1991.
[32] D. Dahihaus, B. H. Fleury, and A. Radović, "A sequential algorithm for joint parameter estimation and multiuser detection in DS/CDMA systems with multipath propagation," *Wireless Personal Commun.*, vol. 6, pp. 161–178, Jan. 1998.
[33] D. Dahlhaus, A. Jarosch, R. Heddergott, and B. H. Fleury, "Joint demodulation of CDMA signals exploiting the time and space diversity of the mobile radio channel," in *Proc. 8th IEEE Int. Symp. Personal, Indoor and Mobile Radio Communications PIMRC'97*, vol. 1, Helsinki, Finland, Sept. 1997, pp. 47–52.
[34] H. L. van Trees, *Detection, Estimation, and Modulation Theory*, vol. I. New York: Wiley, 1968.
[35] S. U. Pillai, *Array Signal Processing*. New York: Springer Verlag, 1989.
[36] P. Stoica and A. Nehorai, "MUSIC, maximum likelihood, and Cramér–Rao bound: Further results and comparisons," *IEEE Trans. Acoust., Speech, Signal Processing.*, vol. 38, pp. 2140–2150, Dec. 1990.

Bernard H. Fleury (M'97) was born in Porrentruy, Switzerland, in 1954. He received the diploma in electrical engineering and mathematics in 1978 and 1990, respectively, and the doctoral degree in electrical engineering in 1990 from the Swiss Federal Institute of Technology Zurich (ETHZ), Switzerland.

During 1978–1985 and 1988–1992 he was a Teaching and Research Assistant at the Communication Technology Laboratory (CTL) and at the Statistics Seminar, respectively, at ETHZ. In 1992 he joined the CTL again where he headed the Spread Spectrum Team from 1994 on. In 1996 he spent seven months as a Research Professor at Center for PersonKommunikation (CPK), Aalborg University, Denmark. Since 1997 he is a Guest Professor in Digital Communication at CPK. His current fields of interest include stochastic modeling of the mobile radio channel, high-resolution methods for the estimation of the radio channel, advanced techniques for joint channel parameter estimation, and detection/decoding in spread spectrum multi-user communication systems.

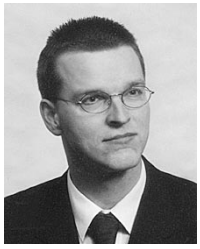

Martin Tschudin (S'96) was born in Basel, Switzerland, in 1969. He received the diploma degree in electrical engineering (Dipl.El.-Ing.) from the Swiss Federal Institute of Technology Zurich (ETHZ), Switzerland, in 1993.

Since 1993, he has been with the Communication Technology Laboratory at ETHZ, where he is currently working as a Research Engineer and is a Ph.D. student. His present research interests include parameter estimation, statistical signal and array processing, and propagation studies of mobile radio channels.

Ralf Heddergott (S'98) was born in Leinefelde, Germany in 1967. He received the Dipl.-Ing. degree in electrical engineering from the University of Kaiserslautern, Germany, in 1995.

Since then, he has been Research Engineer with the Communication Technology Laboratory at the Swiss Federal Institute of Technology Zurich (ETHZ), where he is also studying for the Ph.D. degree. His present research interests are parameter estimation and stochastic modeling of mobile radio channels.

Dirk Dahlhaus (M'93) was born in Essen, Germany, in 1965. He received the Dipl.-Ing. degree in electrical engineering from the Ruhr-Universität Bochum, Germany, in 1992, and the Ph.D. degree in technical sciences from the Swiss Federal Institute of Technology Zurich (ETHZ), Switzerland, in 1998.

Since 1992 he has been with the Communication Technology Laboratory at ETHZ, where he is currently a Senior Researcher in the field of mobile radio signal processing techniques, demodulation schemes in multiuser communications, and implementation issues in third-generation mobile radio systems.

Klaus Ingeman Pedersen (S'97) received the M.Sc. degree in electrical engineering in 1996 from Aalborg University, Denmark. The M.Sc. thesis was completed at wireless information network laboratory (WINLAB), Rutgers University, Piscataway, NJ.

During 1996 he worked at Lucent Technologies Bell Labs innovations where he was involved in the design of wideband CDMA receivers. He is currently a Ph.D. student at Center for PersonKommunikation, Aalborg University. His current research interests are channel modeling including both temporal and azimuthal dispersion and receivers using antenna arrays.